The Role of Convectively Generated Rear-Inflow Jets in the Evolution of Long-Lived Mesoconvective Systems

MORRIS L. WEISMAN

National Center for Atmospheric Research, * Boulder, Colorado*

(Manuscript received 3 June 1991, in final form 23 December 1991)

ABSTRACT

In this study, the structure of convectively generated rear-inflow jets and their role in the evolution of long-lived mesoconvective systems are investigated through an analysis of idealized three-dimensional simulations using a nonhydrostatic cloud model. Rear-inflow jets are generated within these systems in response to the upshear-tilting of the convective circulation, as the horizontal buoyancy gradients along the back edge of the expanding system create a circulation that draws midlevel air in from the rear. Within this framework, a wide range of rear-inflow strengths and structures are produced, depending on the magnitude of the ambient convective available potential energy (CAPE) and the vertical wind shear. In general, for environments characterized by weak-to-moderate vertical wind shear and weak-to moderate CAPE, the rear-inflow jet descends and spreads along the surface well behind the leading edge of the gust front, and the subsequent convective activity becomes weaker. However, for environments characterized by strong environmental vertical wind shear and strong CAPE, the rear inflow remains elevated to near the leading edge of the system, and strong, upright convective cells are maintained along the gust front. The influence of the rear-inflow jets on the evolution of these systems is examined through an extension of the recent theory of Rotunno et al., whereby the characteristics of the lifting produced at the leading edge of the system are controlled by the relative balance between the horizontal vorticity generated by the cold pool and the horizontal vorticity that is inherent in both the ambient vertical wind shear and the rear-inflow jet.

1. Introduction

Recent observational and numerical studies have clarified many of the structural and evolutionary characteristics of squall-line-type convective systems. Much of the emphasis has been on understanding the interaction between the narrow band of intense convective cells along the leading edge of the system, which dominates the early portion of the system lifetime, and a wide band of more gradual ascent and stratiform precipitation that develops behind the convective line, which dominates the later portion of the system lifetime (e.g., Zipser 1977; Houze 1977; Houze et al. 1990). As this larger-scale circulation develops, a system-relative current of air is also often observed that feeds into the stratiform precipitation region from the rear at midlevels. These rear-inflow jets (e.g., Smull and Houze 1987) play a crucial role in supplying potentially cold and dry midlevel air to aid in the production of the convective and system-scale downdrafts. However, the impact of these jets on the subsequent evolution

of the convective system as a whole has not yet been clarified.

In the present study, we investigate rear-inflow jets through a series of idealized simulations of convective systems using a three-dimensional nonhydrostatic cloud model. By varying the environmental buoyancy and vertical wind shear over a wide range of conditions, we are able to reproduce many observed rear-inflow characteristics and are able to clarify the environmental controls on rear-inflow strength and structure. Through an analysis of these simulations, we then offer an explanation for how the various jet structures may influence the cold-pool circulation at the leading edge of the convective system, producing stronger or weaker convective circulations.

A schematic depicting many commonly observed features of convective systems with rear-inflow jets is presented in Fig. 1 (from Houze et al. 1989). This figure depicts a squall line during its mature phase of development, consisting of a line of intense convective cells along the leading edge of the system with an extensive stratiform precipitation region extending to the rear. Rear-inflow jets in such systems occur as part of a mesoscale circulation couplet, consisting of ascending front-to-rear flow in the anvil cloud region, which emanates from the leading-edge convective cells, and descending rear-to-front flow below, which can extend from the rear edge of the system and feed through the

---

Corresponding author address: Dr. Morris L. Weisman, National Center for Atmospheric Research, P.O. Box 3000, Boulder, CO 80307-3000.
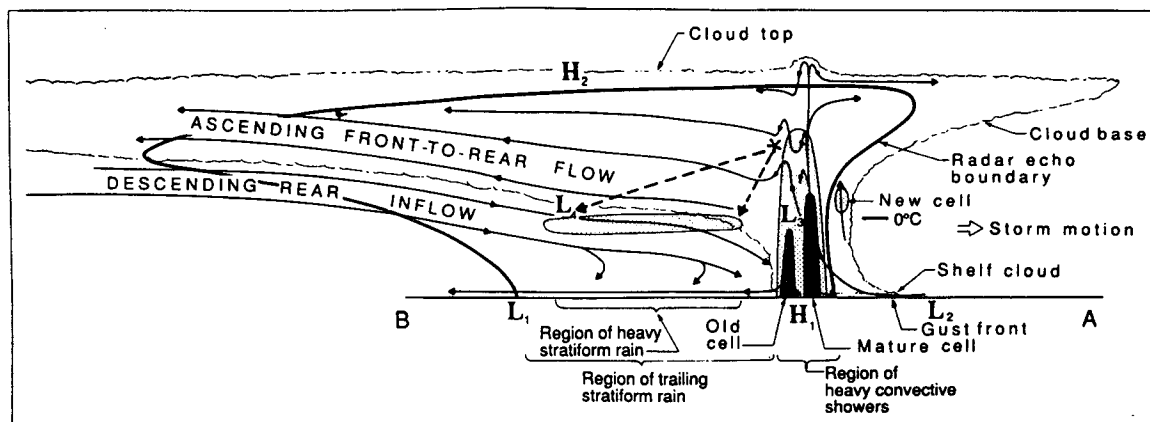
FIG. 1. Conceptual model of a squall line with a trailing stratiform area viewed in a vertical cross section oriented perpendicular to the convective line (i.e., parallel to its motion) (from Houze et al. 1989).

stratiform precipitation and into the surface cold pool. Within this conceptual framework, however, rear-inflow jets exhibit a large variety of structures and strengths. Of the 18 convective systems studied by Smull and Houze (1987), three of the cases were characterized as having strong rear inflow (i.e., greater than 10 m s^{-1} of relative flow across the back edge of the stratiform precipitation region), five had moderate rear inflow (5–10 m s^{-1}), and ten, referred to as stagnation zone cases, had little or no rear inflow.

For some of the stagnation zone cases, weak rear inflow was observed at the back edge of the system, with strong rear inflow observed well within the stratiform region, close to the leading-edge convection. An example of this latter behavior is also presented by Chong et al. (1987), who discuss a long-lived squall line for which the rear inflow increased to over 15 m s^{-1} close to the active convective zone. Cases such as this lead Smull and Houze (1987) to hypothesize that rear-inflow jets may be generated by the convective system itself, as opposed to being the manifestation of upstream variations in the preconvective winds. Based on the previous results of LeMone (1983) and LeMone et al. (1984), they suggested that the acceleration of the flow may be due to a hydrostatically induced perturbation pressure minimum that develops under the warm convective updraft current that slopes over the cold surface outflow. However, the lack of observations that document the evolution of these features precludes any definitive conclusions concerning their origin in most observational cases. This information may be crucial to understanding the relative importance of larger-scale versus convective-scale processes in the evolution of such convective systems.

The apparent role of the rear-inflow jets in the evolution of these convective systems also varies considerably from case to case. For the 22 May 1976 case discussed by Smull and Houze (1987) and Ogura and Liou (1980), and for the 10–11 June case discussed

by Smull and Houze (1987) and Rutledge et al. (1988), among many others, the appearance of intense rear inflow coincided with a noticeable weakening of the active convective zone and a slow dissipation of the system as a whole. However, for the 28 May 1985 case discussed by Smull and Houze (1987) and Houze et al. (1989) and for the case discussed by Chong et al. (1987), the leading-edge convective cells and overall system circulation remained strong for many hours after the development of the rear inflow. Smull and Houze (1987) noted that the rear-inflow current 50 km behind the leading edge of the system was much deeper on 28 May than on 10 June (5 km versus 3 km) and suggest that this might be important for explaining the relative lack of stratiform precipitation observed on 28 May. Similarly, Chong et al. (1987) also noted an unusual depth of the rear-inflow current feeding to immediately behind the convective zone for their case. As we will propose, this distinction may be crucial to understanding the interaction between the rear-inflow and the convective system. Another significant issue for many of these cases is that the rear-inflow structure and attendant convective structures vary considerably along the extent of the convective system, suggesting that three-dimensional aspects of the flow may be important for interpreting the structure and influence of the rear-inflow jets.

Numerical simulations of squall lines regularly produce enhanced rear inflows as part of the natural evolution of the convective system (e.g., Lafore and Moncrieff 1989; Fovell and Ogura 1989; Weisman et al. 1988). In such cases, the rear inflow is generated as the convective system evolves from a narrow band of intense convective cells to a broader band of more gradual ascent and stratiform precipitation. This transition in structure is a consequence of the intensification and deepening of the convectively generated cold pool, as described by Rotunno et al. (1988, hereafter RKW), and is represented schematically in Fig. 2. Ini-
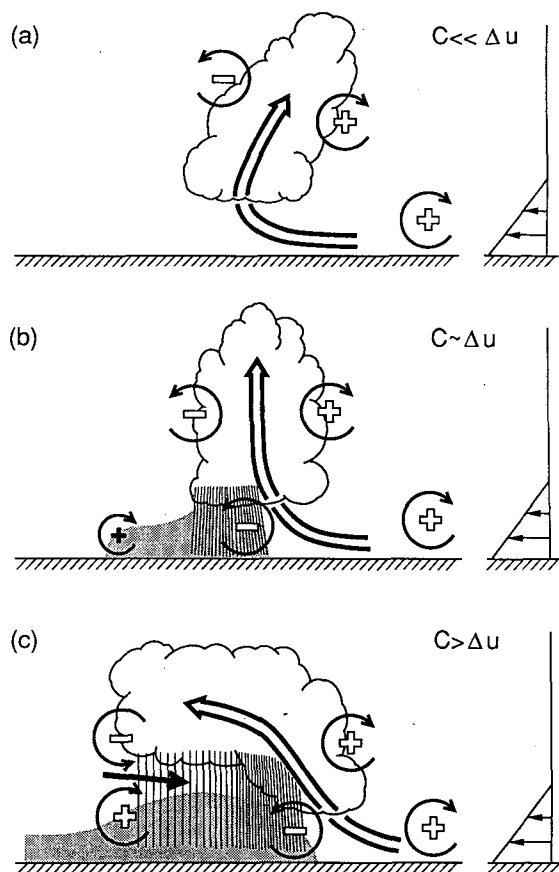
FIG. 2. Three stages in the evolution of a convective system. (a) An initial updraft leans downshear in response to the ambient vertical wind shear, which is shown on the right. (b) The circulation generated by the storm-induced cold pool balances the ambient shear, and the system becomes upright. (c) The cold-pool circulation overwhelms the ambient shear and the system tilts upshear, producing a rear-inflow jet. The updraft current is denoted by the thick, double-lined flow vector, with the rear-inflow current in (c) denoted by the thick, solid vector. The shading denotes the surface cold pool. The thin, circular arrows depict the most significant sources of horizontal vorticity, which are either associated with the ambient shear or are generated within the convective system, as described in the text. Regions of lighter or heavier rainfall are indicated by the more sparsely or densely packed vertical lines, respectively. The scalloped line denotes the outline of the cloud; C represents the strength of the cold pool, while Δu represents the strength of the ambient low-level vertical wind shear, as described in the text.

tially, a convective cell evolving in a vertically sheared environmental flow leans downshear in response to the ambient vertical wind shear (Fig. 2a). As a cold pool develops beneath the convection, the horizontal buoyancy gradients along the edge of the cold pool generate circulation that, along the downshear edge of the cold pool, is of the opposite sense as the circulation inherent in the ambient shear. When this cold pool circulation balances the circulation inherent in the ambient shear, deep lifting is produced at the cold pool edge, resulting in the production of strong, upright convective cells

(Fig. 2b). RKW refer to this state as "optimal" for the maintenance of strong, long-lived squall lines. As the cold pool circulation continues to strengthen, it eventually overwhelms the ambient shear, and the convective circulation begins to tilt rearward over the cold air (Fig. 2c). This represents the beginning phase in the development of the trailing stratiform precipitation region.

It is during this upshear-tilting phase of the system that significant rear-inflow jets are characteristically generated. As described by Lafore and Moncrieff (1989), this occurs as the horizontal buoyancy gradients along the rear edge of the buoyant plume aloft and cold pool near the surface generate horizontal vorticity, thereby accelerating the flow from rear to front at midlevels (as indicated in Fig. 2c by the bold arrow between the positive and negative circulation couplet at the back edge of the system). This mechanism is equivalent to that proposed by LeMone (1983) and LeMone et al. (1984), in that this configuration of the buoyancy field also implies a minimum in the hydrostatic pressure field at midlevels (between the warm plume aloft and the cold pool at the surface) that accelerates the rear-inflow current. Lafore and Moncrieff and Fovell and Ogura (1989) both document a systematic increase in the strength of this convectively generated rear inflow for increasing magnitudes of the ambient low-level vertical wind shear for idealized two-dimensional squall-line simulations. In addition, Lafore and Moncrieff also document an increase in rear inflow strength for increasing magnitudes of the ambient convective available potential energy (CAPE). However, neither of these studies offers a physical explanation for these rear-inflow properties.

As with the observational studies, these numerical simulations also suggest a wide range of potential interactions between the rear-inflow jet and the convective system. For instance, Lafore and Moncrieff hypothesized that a rear-inflow current that descends to the surface may increase the surface convergence along the gust front, thereby enhancing the convective system through the triggering of new convective cells. They also suggested, however, that if the subsidence behind the convective system is too strong, then the overall rear-to-front circulation will be lowered and may be less efficient in releasing the convective instability.

Fovell and Ogura (1989) and Fovell (1991) hypothesized that a stronger rear inflow could tend to advect more dry air into the mesoscale downdraft region in the trailing portion of the convective system, leading to enhanced evaporation and an enhanced cold pool. This enhanced cold pool could produce more of an imbalance with the ambient vertical wind shear, as described by RKW, resulting in a weaker system. In point of fact, though, the strongest convective systems in the Fovell and Ogura study were associated with the strongest cold pools and rear-inflow jets, suggesting that the RKW theory alone could not account for the system

behavior. Also, in contrast to the first hypothesis of Lafore and Moncrieff, the strongest convective systems in this study were associated with rear-inflow jets that remained elevated to near the leading edge of the system rather than descending and spreading along the surface some distance behind the leading edge. Thus, surface convergence alone is also not sufficient to explain the observed convective behavior.

In the following, we will attempt to clarify these issues by investigating the evolution of rear-inflow jets within fully three-dimensional convective systems. Our goal is to document more clearly the environmental factors affecting the structure and strength of the rear-inflow jets, as well as to clarify the role they play in the subsequent evolution of the convective system. As in the previous numerical studies, we are interested specifically in the properties of convectively generated rear inflows. Consequently, the convection will be simulated in initially horizontally homogeneous conditions. We will present results for a wide range of ambient buoyancy and vertical wind-shear conditions, but we will concentrate especially on two of the simulations that clarify much of the range of rear-inflow properties. In both cases, significant midlevel rear-inflow jets develop by two-to-three hours into the lifetime of the system. In the first case, characterized by moderate environmental vertical wind shear, the rear inflow descends and spreads along the surface well behind the leading edge of the system, and the subsequent convective activity becomes weaker. In the second case, characterized by strong environmental vertical wind shear, the strongest rear inflow remains elevated to near the leading edge of the system, and strong, upright convective cells are maintained along the gust front.

We will begin with a description of these two primary simulations. We will then present an analysis using the horizontal vorticity equation that reveals the processes important to the generation of the rear-inflow jets and clarifies the factors that tend to produce jets that remain elevated as opposed to those that descend and spread along the surface. We will then review the recent theory of RKW and propose an extension to the theory to explain the effects of rear inflows on the strength and longevity of convective systems. Finally, we will generalize these results to the full range of buoyancy and vertical wind shear conditions simulated and will discuss them in light of the observational and numerical evidence already presented in the literature.

2. Experimental design

The simulations to be discussed in this paper were completed using the Klemp and Wilhelmson (1978) numerical cloud model, as used by Weisman et al. (1988, hereafter WKR). In order to simplify the interpretation of the results, the present model formulation does not include ice processes, radiation, or the Coriolis force. These processes may all have significant impacts on long-term simulations (i.e., 6 hours or more), but previous studies (e.g., Fovell 1991) suggest they do not significantly affect the results for simulations of 4 hours or less, as used in the current study. A free-slip condition is used at the lower boundary, with an open boundary condition specified at the lateral boundaries and a radiation-type condition specified at the top of the domain.

Each simulation is initialized in a horizontally homogeneous environment that is characterized by specified vertical profiles of temperature, water vapor, and wind. In addition, the initial wind profiles are unidirectional. With the Coriolis force set to zero, these conditions ensure a mirror-image symmetry to the solution about an axis directed parallel to the vertical wind-shear vector. Thus, only half of the full domain need be included. Storms are initialized by placing an ellipsoidal warm thermal of 10-km horizontal and 1400-m vertical radius on the center of the symmetry axis. The thermal is given a maximum magnitude of $2°C$ at the center, which decreases to zero at the edge, and is balanced hydrostatically with the pressure field. Air accelerates horizontally into the region of lowered pressure beneath the thermal, with the resultant convergence creating upward motion that releases the convective instability. The simulations to be described all use a horizontal grid resolution of 2 km and a vertical grid resolution of 750 m. The domain size is 80 km in the y, or cross-wind direction, 160 km in the x, or along-wind direction, and 17.5 km in the z, or vertical direction. The symmetry axis is located along $y = 0$, and thus the effective domain size in the y direction is 160 km. Each simulation is run for 240 min.

The thermodynamic profiles used in this study are presented in Fig. 3, with the associated quantitative characteristics included in Table 1. The CAPE is varied by changing both the slope of the temperature profile and the magnitude of the low-level mixing ratio. This produces a range of CAPE of between 1182 and 3847 $m^2 s^{-2}$, which covers much of the observed range of environments associated with significant midlatitude and tropical convective systems. The mixing ratio in the lowest 50–100 mb is varied between 13 and 14 $g kg^{-1}$ from case to case, but the moisture profile above this level remains constant for all of the experiments, generally representing moist mid- and upper-level conditions. Future studies will consider variations to these conditions as well. The ambient wind profile for each experiment consists of linear, unidirectional vertical shear from the surface to either 2.5 km or 5 km AGL, with constant winds above. The maximum magnitude of the wind at the top of the shear profile (U_s) is varied from 0 to 30 m s^{-1} for the 2.5-km cases and 0 to 40 m s^{-1} for the 5-km cases. At the beginning of each simulation, a mean storm speed is subtracted from the initial wind profile to keep the convective system near the center of the model domain.
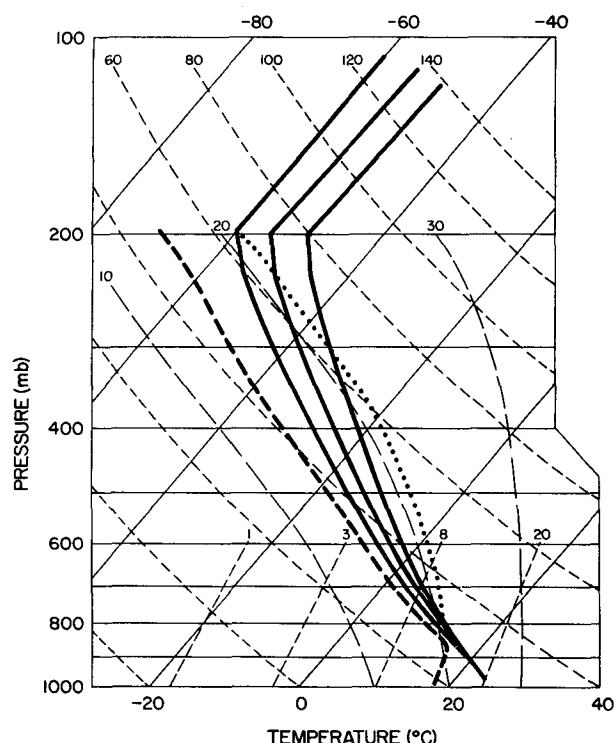
FIG. 3. Skew T–log p diagram depicting the range of thermodynamic profiles used for the numerical simulations. The three temperature profiles are depicted by the thick, solid lines, while the moisture profile is depicted by the thick, dashed line. The thick, dotted line represents the parcel ascent curve for the 14 g kg^{-1} surface mixing ratio cases included in Table 1.

3. General system characteristics

The two simulations to be described in detail in the next few sections are both initialized with a CAPE of 2377 m^2 s^{-2} (case 3 in Table 1), with the first considering an environment with U_s = 15 m s^{-1} over the lowest 2.5 km AGL (referred to as the moderate-shear simulation) and the second considering an environment with U_s = 25 m s^{-1} over the same depth (referred to as the strong-shear simulation). The structure of the rear-inflow jet produced in the moderate-shear case is also representative of weaker-shear simulations, except that the rear inflow decreases in magnitude for weaker shears.

The evolution of these two cases follows closely the general evolution described in the Introduction. By one hour, the initial cells generate a cold pool that spreads against the relative surface inflow. New cells are generated along the downshear portion of the cold pool, creating an arc of cells propagating in the direction of the low-level shear. These new cells deepen and strengthen the cold pool by producing an additional downward transport of low θ_e from midlevels that is cooled through the evaporation of rain. Eventually, the cold pool-generated circulation forces the convective

elements to propagate upshear relative to the cold-pool edge. As this occurs, a rear-inflow jet develops that subsequently influences the circulation at the leading edge of the system.

The key aspects of this evolution are presented through a series of vertical cross sections in Figs. 4 and 6 (for the moderate- and strong-shear cases, respectively) that display system-relative flow vectors, rainwater concentration, and θ_e along the symmetry axis of the model domain at hourly intervals through 240 min. In addition, horizontal cross sections are presented in Figs. 5 and 7 at 180 min that display the rainwater concentration and system-relative flow at 0 and 2.5 km AGL along with the location of the surface gust front to clarify the three-dimensional characteristics of the system structure. For the moderate-shear simulation, the circulation at 60 min (Fig. 4a) is dominated by a single, mature rain cell, with the primary updraft extending between 5 and 12 km AGL and the downdraft located beneath. The updraft is characterized by high values of θ_e, having originated in the surface layer ahead of the system, while the downdraft is characterized by low θ_e air, having originated at midlevels on the downshear side of the cell. As discussed by RKW, this downshear origin of the downdraft during the early stages of system development is characteristic of convection growing in vertically sheared environments. This low θ_e air spreads along the surface in the form of a cold pool, which has triggered a new updraft cell as a result of the convergence along its downshear edge.

By 120 min (Fig. 4b), the updraft portion of the circulation has become tilted upshear, with both the original and new convective cells having weakened and advected rearward relative to the leading edge of the surface cold pool. Low θ_e air associated with the downdraft has also begun to originate more from the rear of the system at midlevels. This circulation continues to expand and intensify, and by 180 min (Fig. 4c), the system is composed of a broad, gradually ascending updraft current extending rearward above the cold pool and a rear-inflow current descending and spreading along the surface well behind the leading edge of the gust front. The horizontal cross sections at 180 min (Fig. 5) depict a 70-km-long line of weak convective cells (including the upper portion of the symmetric

TABLE 1. Conditions for the five case studies.

Case	Low-level mixing ratio (g kg^{-1})	Cloud base (m)	Level of free convection (m)	CAPE (m^2 s^{-2}) Negative	CAPE (m^2 s^{-2}) Positive
1	14	1107	1907	−17	1182
2	13	1252	1952	−16	1795
3	14	1107	1707	−12	2377
4	13	1252	1752	−10	3187
5	14	1107	1507	−6	3847

MODERATE-SHEAR SIMULATION
($U_s = 15 \text{ m s}^{-1}$)

(a) 60 Min

(b) 120 Min
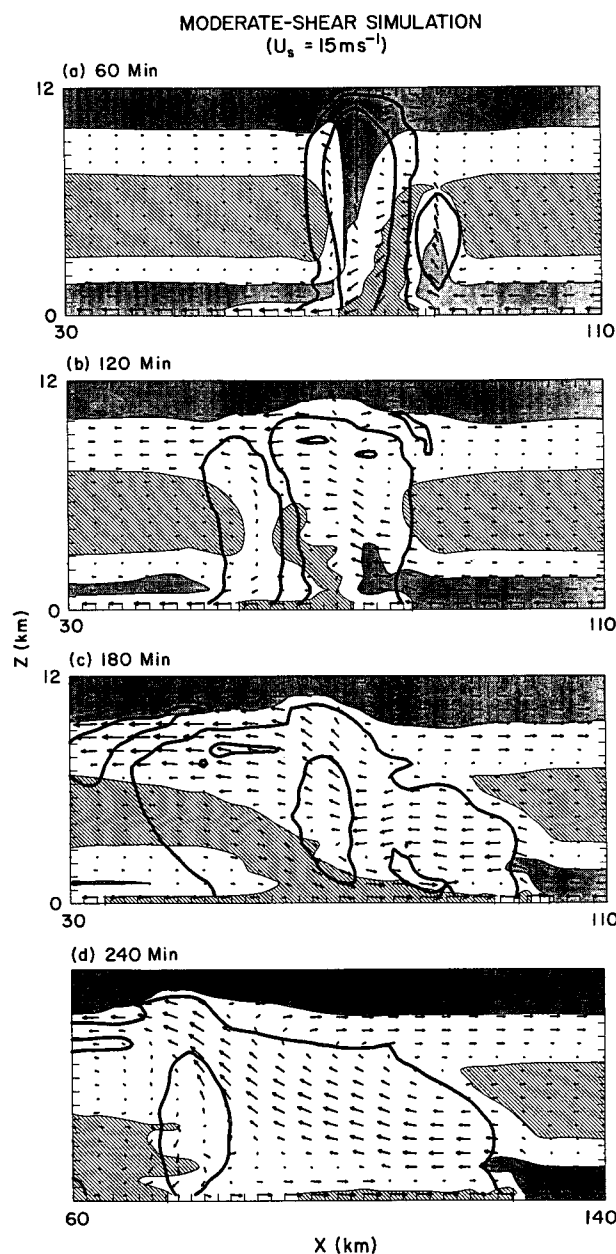
(c) 180 Min

(d) 240 Min

X (km)

FIG. 4. Vertical cross sections of θ_e, flow vectors (approximately storm-relative), and rainwater concentration along the $y = 0$ boundary at (a) 60 min, (b) 120 min, (c) 180 min, and (d) 240 min for the moderate-shear simulation. Vectors are presented at every other grid point, with a vector length of two grid intervals being equal to a magnitude of 25 m s^{-1}. A domain speed of $u = 16$ m s^{-1} is subtracted from the flow field. Regions of θ_e greater than 334 K are darkly shaded, and regions less than 326 K are lightly shaded. Thick lines represent the 0 and 4 g kg^{-1} rainwater contours. Only an 80 × 12 km portion of the domain is presented.

MODERATE-SHEAR SIMULATION
($U_S = 15 \text{ m s}^{-1}$)

T = 180 Min
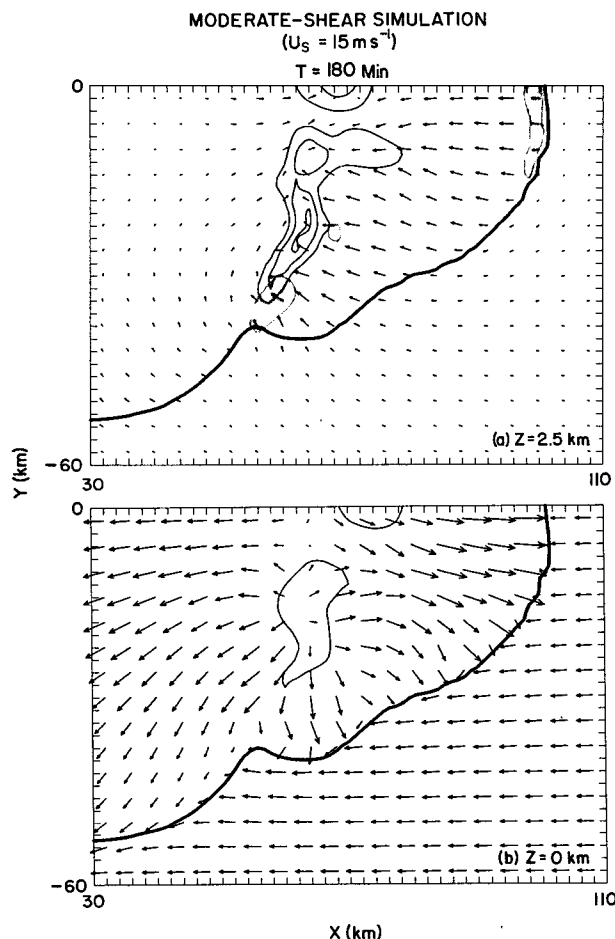
Y (km)

(a) Z = 2.5 km

(b) Z = 0 km

X (km)

FIG. 5. Horizontal cross sections of rainwater concentration and flow vectors (approximately storm-relative) at (a) 2.5 km AGL and (b) 0 km AGL at 180 min for the moderate shear simulation. Vectors are presented at every other grid point, with a vector length of two grid intervals being equal to a magnitude of 25 m s^{-1}. A domain speed of $u = 16$ m s^{-1} is subtracted from the flow field. The rainwater is contoured at 2 g kg^{-1} intervals, and the thick line represents the location of the gust front at the surface. For (a), regions of updraft greater than 4 m s^{-1} are shaded. The $y = 0$ boundary represents the axis of symmetry for the simulation, with only a 60 × 80 km portion of the full domain presented.

domain, not shown) located up to 35 km behind the leading edge of the gust front near the center of the system, with relatively uniform rear-to-front system-relative flow at the surface extending between the cells

and the gust front and front-to-rear flow at 2.5 km AGL above this surface flow. This general configuration is maintained through 240 min (Fig. 4d), with a broad, shallow updraft current continuing to expand rearward above the spreading cold pool.

The initial evolution of the strong-shear case is similar to that described above, except that at 120 min (Fig. 6b) a strong, erect updraft and rain cell is still evident at the leading edge of the gust front. Low θ_e air has again begun to enter the downdraft at midlevels from the rear of the system, but there has been much less of a tendency for the convective cells to advect rearward above the surface cold pool. However, by 180 min (Fig. 6c), the rain field has expanded 50 km behind
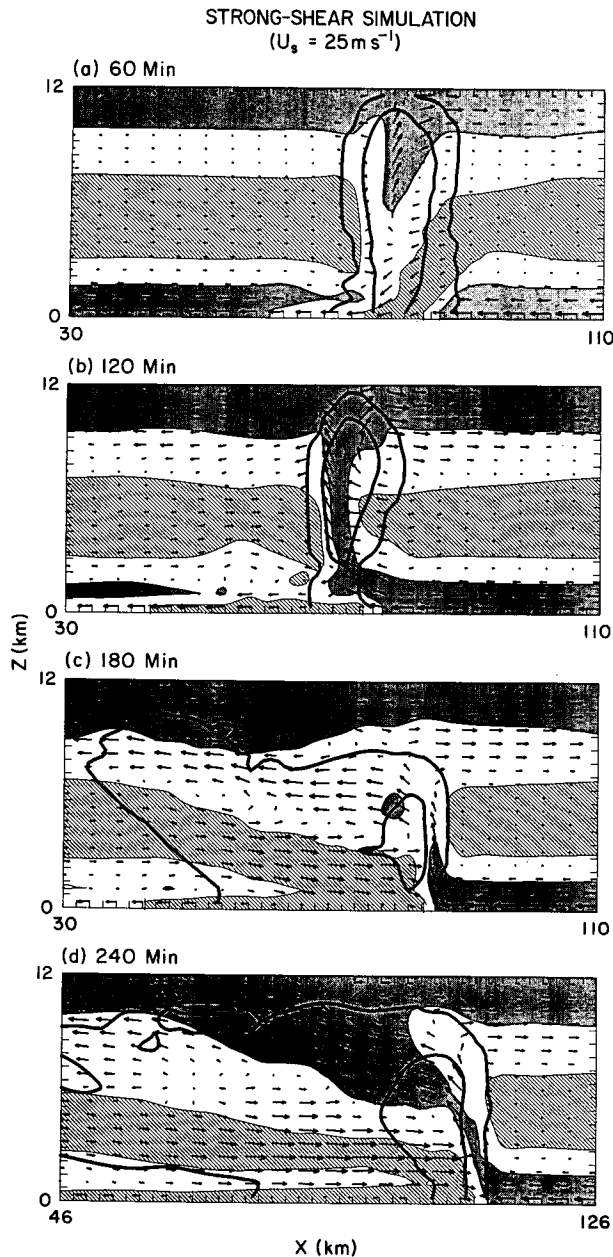
STRONG-SHEAR SIMULATION
(U_s = 25 m s^{-1})

FIG. 6. As in Fig. 4 except for the strong-shear simulation. A domain speed of u = 22.5 m s^{-1} is subtracted from the flow field.

STRONG-SHEAR SIMULATION
(U_S = 25 m s^{-1})
T = 180 Min

FIG. 7. As in Fig. 5 except for the strong-shear simulation. A domain speed of u = 22.5 m s^{-1} is subtracted from the flow field.

the leading edge of the system, with a strong front-to-rear current of high θ_e air having developed above 5 km AGL and a strong rear-inflow jet feeding low θ_e air from midlevels into the downdraft beneath it. Unlike the moderate-shear case, however, the strongest rear-inflow remains elevated at 2 to 3 km AGL to near the leading edge of the gust front, with a strong convective cell still evident at that location.

The horizontal cross sections at 180 min (Fig. 7) depict a convective line segment that extends over 80
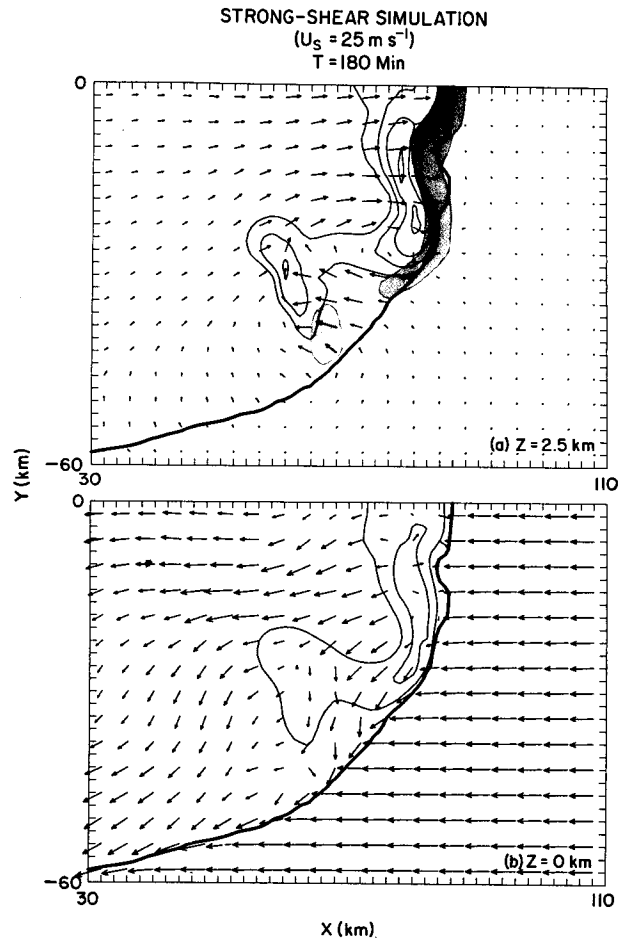
km in length, with intense updrafts and rain cells situated along most of the leading edge of the gust front. The surface flow (Fig. 7b) is characterized by a narrow band of system-relative rear-to-front flow just behind the gust front, but primarily front-to-rear flow extending to the rear of the gust front. At 2.5 km (Fig. 7a), system-relative rear inflow extends behind most of the convective line and accelerates to nearly 20 m s^{-1} as it approaches the leading edge of the gust front. A cyclonic vortex is evident at the southern edge of the rear-inflow current, with a mirror-image anticyclonic vortex also evident at the northern edge (not shown). This system strengthens further over time, with a strong, elevated rear-inflow jet still impinging to near the leading edge of the gust front at 240 min (Fig. 6d) and a strong convective cell still evident at that location.

The general uniformity of the flow field within the central 40–60-km section of the convective systems for both the moderate- and strong-shear simulations at 180 min (Figs. 5 and 7) suggests that the processes responsible for the development of the vertical circulations

depicted in Figs. 4 and 6 are largely two-dimensional. Further analyses (not shown) indeed confirm this and show that the primary contribution to the rear-inflow momentum within this region comes from accelerations due to a quasi–two-dimensional buoyancy-induced pressure minimum at midlevels above the cold pool, as described, for example, by Lafore and Moncrieff (1989). This process of rear-inflow generation is discussed in more detail in the following section. The only significant departure from this two dimensionality occurs for the strong-shear simulation after 180 min, as the vortices evident at the ends of the convective system in Fig. 7a draw closer to the core of the system and contribute as much as 40%–50% of the observed rear-inflow strength at that location. The three-dimensional structure and longevity of this strong-shear system is similar to observational studies of long-lived bow-echoes (e.g., Fujita 1978) and is discussed in more detail in a companion paper by Weisman (1992). The present analysis will concentrate on the development of the rear-inflow within the core region of the convective systems through 180 min, when the two-dimensional assumptions are still largely valid.

For the discussions to follow, it will be useful to interpret the evolution of these two cases within the context of the cold pool–vertical shear balance relationship developed by RKW, as discussed in the Introduction. This relationship may be expressed quantitatively in the form of a ratio, $C/\Delta u$, where C represents the cold-pool strength and Δu represents the velocity difference between the surface and 2.5 km in the ambient air ahead of the cold pool. Here, C is defined via

$$C^2 = 2 \int_0^H (-B)dz, \qquad (1)$$

where B represents the buoyancy, defined as

$$B \equiv g\left[\frac{\theta'}{\bar{\theta}} + 0.61(q_v - \bar{q}_v) - q_c - q_r\right], \qquad (2)$$

and where θ is the potential temperature and q_v, q_c, and q_r are the mixing ratios of water vapor, cloudwater, and rainwater, respectively. The integral is calculated through the depth of the cold pool (H) at a representative location behind the cold-pool nose (i.e., avoiding the region of internally enhanced cold pool depth right at the leading edge). During the initial phases of a storm, the cold pool is characteristically weak. Thus, $C/\Delta u$ is much less than 1, and the circulation inherent in the vertical wind shear overwhelms the cold-pool circulation, causing the system to tilt downshear (Fig. 2a). As the cold pool strengthens, $C/\Delta u$ approaches an optimal value of 1, and strong, upright cells are produced along the leading edge of the cold pool (Fig. 2b). As the cold pool continues to strengthen, $C/\Delta u$ becomes greater than 1, and the system begins to tilt upshear and weaken (Fig. 2c).

A time series of $C/\Delta u$ for the two simulations is presented in Fig. 8a, along with a time series of the maximum strength of the rear inflow at 2.5 km AGL (presented relative to the ambient 2.5-km flow) in Fig. 8b. For the moderate shear case, $C/\Delta u$ becomes greater than 1 by 60 min, suggesting that the system should tilt upshear and weaken relatively quickly. This is indeed what is observed, and the development of a rear-inflow jet that descends and spreads along the surface after 120 min does not appear to alter this evolution. For the strong-shear simulation, $C/\Delta u$ increases to greater than 1 after 120 min, and, as expected, the circulation also begins to spread upshear. However, the concurrent generation of the elevated rear-inflow jet for this case appears to alter the evolution predicted by RKW, with an intense, erect updraft maintained at the leading edge of the system despite a continuing and increasing imbalance between the cold pool and ambient low-level vertical wind shear. In the following sections, we will discuss the mechanisms responsible for the generation of these different jet structures and offer a theory for how the rear-inflow jets can be incorporated into the RKW theory to explain the resultant system evolutions.

4. The generation of elevated versus descending midlevel jets

The forcing mechanisms important to the generation of the different jet structures may be analyzed through
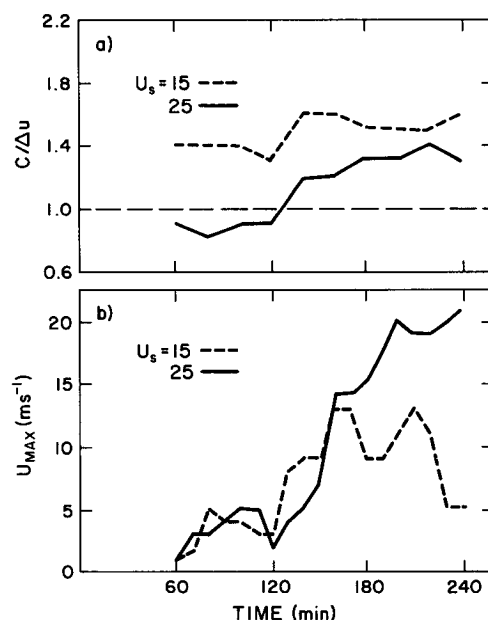

FIG. 8. Time series of (a) $C/\Delta u$ and (b) maximum midlevel rear inflow strength on the symmetry axis (as described in the text) for the moderate- (dotted line) and strong-shear (solid line) simulations.

the use of the two-dimensional horizontal vorticity equation

$$\frac{d\eta}{dt} = -\frac{\partial B}{\partial x}, \quad (3)$$

where $\eta = \partial u/\partial z - \partial w/\partial x$ and where B represents the buoyancy, defined by (2). The only source of horizontal vorticity in this two-dimensional framework is horizontal gradients of buoyancy. The analysis of the development of circulation is thus simplified to understanding the evolution of the buoyancy field.

In order to investigate the development of the rear-inflow jets, vertical cross sections of the full buoyancy field as defined by (2) and the pressure perturbation field, along with vertical cross sections of the system relative flow vectors and the horizontal buoyancy-gradient field, are presented at 120, 140, 160, and 180 min in Figs. 9 and 10. This represents the time period when the forcing of the jets is clearly evident. For the moderate-shear case, the buoyancy field at 120 min (Fig. 9a) is characterized by the cold pool at the surface, with a buoyant updraft above it. A region of relatively low pressure is located just below this buoyant plume, at the top of the cold pool, with relatively high pressure evident at the surface within the cold pool. This buoyant plume aloft and associated mesolow at midlevels expands rearward over the next 60 min, with the rear-inflow jet accelerating in response to this developing system-scale pressure field (Fig. 10).

The buoyancy-gradient field (Fig. 10) depicts a region of strong negative vorticity forcing along the leading edge of the cold pool throughout the analysis period (labeled A on the figure). At 120 min (Fig. 10a), there is also a region of weaker positive vorticity forcing along the back side of a deeper portion of the rearward-spreading cold pool (B) along with a region of weaker negative vorticity forcing aloft (C) associated with the back edge of the warm plume aloft. These latter two regions of vorticity forcing advect rearward between 120 and 160 min (Figs. 10b,c) and coincide with the primary generation zone for the descending midlevel rear-inflow current. As this rear-inflow descends toward the surface, it is enhanced further by an additional zone of weak negative vorticity forcing (D) associated with the weak positive buoyancy gradient extending forward from the deepest portion of the cold pool located toward the rear of the system. This deeper portion of the cold pool is also collocated with the highest surface pressure, and the enhancement in the rear-inflow momentum can be interpreted equivalently as an acceleration in response to the associated enhanced surface pressure gradient.

The cross sections for the strong-shear case indicate a similar pattern, except that the cold pool at the surface and the buoyant plume aloft are both of greater magnitude (Fig. 11). Accordingly, there is also a much stronger mesolow above the cold pool and mesohigh

at the surface. The buoyancy-gradient field (Fig. 12) still depicts a region of negative vorticity forcing at the leading edge of the cold pool (A) but now shows strong, nearly equal magnitudes of both positive (B) and negative (C) vorticity forcing within the generation zone of the rear-inflow jet along the rear edge of the expanding system. In this case, the deepest portion of the cold pool remains located near the leading edge of the system, so that the surface vorticity forcing zone D that was apparent in the moderate-shear case (Fig. 10) now does not appear distinct from zone A in Fig. 12. However, in both cases, the forcing for the midlevel rear-inflow current is associated primarily with the horizontal gradients of buoyancy located along the back edge of the upshear-spreading system, as previously discussed by Lafore and Moncrieff (1989).

In order to explain the production of the elevated versus descending jet, we offer a simple analogy from fluid dynamics. Within a two-dimensional framework, a symmetric jet of air may be created by placing two circular regions of vorticity forcing of equal size and magnitude but opposite sign in close proximity to each other. However, if the magnitude or size of the vorticity-forcing regions is such that the integrated effect in the two zones is not equal, the resultant jet of air will be deflected in the direction of the stronger vorticity forcing. In the strong-shear case discussed above, the buoyancy gradients (and the net integrated effect of the buoyancy gradients) associated with the buoyant plume aloft are equal or greater in magnitude than the buoyancy gradients associated with the rearward portion of the cold pool during most of the period of jet formation. In this case, the jet remains elevated. For the moderate-shear simulation, the cold-pool gradients are similar to those produced in the strong-shear simulation, but the buoyancy gradients aloft are much weaker, and the jet descends rapidly to the surface.

These results suggest that the production of an elevated rear-inflow jet depends on the production of strong horizontal gradients of buoyancy associated with the positively buoyant plume spreading rearward above the cold pool. The buoyancy gradient, in turn, depends on the magnitude of the buoyancy within the rearward-spreading plume. Both the buoyancy and the buoyancy gradients in the moderate-shear simulation are less than those realized in the strong-shear case. Since identical thermodynamic profiles are used in each of these simulations, an explanation must be offered to account for these different buoyancy characteristics.

The amount of buoyancy realized by a surface parcel lifted in a convectively unstable environment depends on both the potential temperature excess created by the lifting process and the amount of water that accumulates within the parcel. If a series of parcels is continually lifted within a given vertical column, then the amount of buoyancy that will be realized by any given parcel is difficult to estimate as water begins to accumulate and fall through the column. If a series of

MODERATE-SHEAR SIMULATION
BUOYANCY, ρ'

(a) 120 Min

(b) 140 Min

(c) 160 Min

(d) 180 Min

X (km)

MODERATE-SHEAR SIMULATION
VECTORS, −∂B/∂X

(a) 120 Min

(b) 140 Min

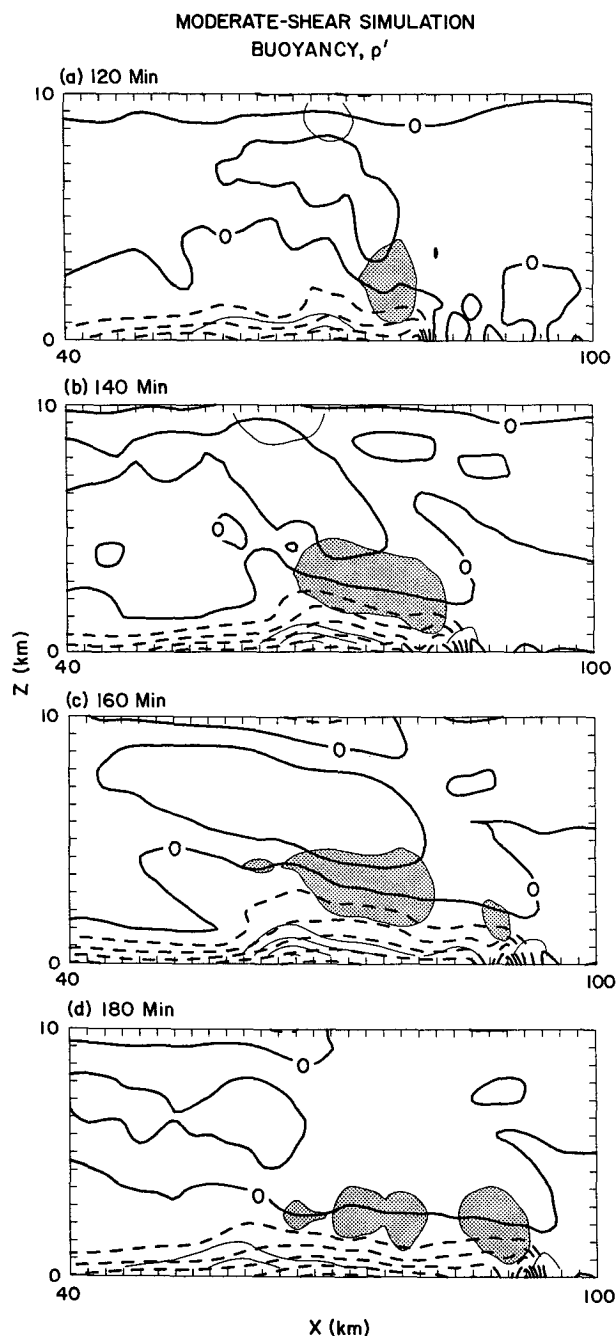(c) 160 Min

(d) 180 Min

X (km)

FIG. 9. Vertical cross sections along the $y = 0$ axis, depicting the buoyancy field (thick lines) and pressure perturbation field (thin lines) at (a) 120, (b) 140, (c) 160, and (d) 180 min for the moderate-shear simulation. The buoyancy field is contoured using a 600 $\times 10^{-4}$ m s^{-2} interval, and the pressure field is contoured using a 0.75-mb interval with the zero contour omitted. Negative pressure perturbations are shaded starting at −0.75 mb. Only a 60 × 10 km portion of the full domain is presented.

FIG. 10. Vertical cross sections along the $y = 0$ axis, depicting flow vectors (approximately storm-relative) and the buoyancy-gradient field ($-\partial B/\partial x$) at (a) 120, (b) 140, (c) 160, and (d) 180 min for the moderate-shear simulation. The buoyancy-gradient field is contoured using a 10 × 10^{-6} s^{-2} interval, with the zero contour omitted. One grid interval represents a vector magnitude of 25 m s^{-1}. A domain speed of $u = 16$ m s^{-1} has been subtracted from the flow field. Only a 60 × 10 km portion of the full domain is presented.

parcels is lifted in a strongly tilted updraft, however, then the rainwater falls out of the updraft plume, and the amount of buoyancy realized is more directly re-
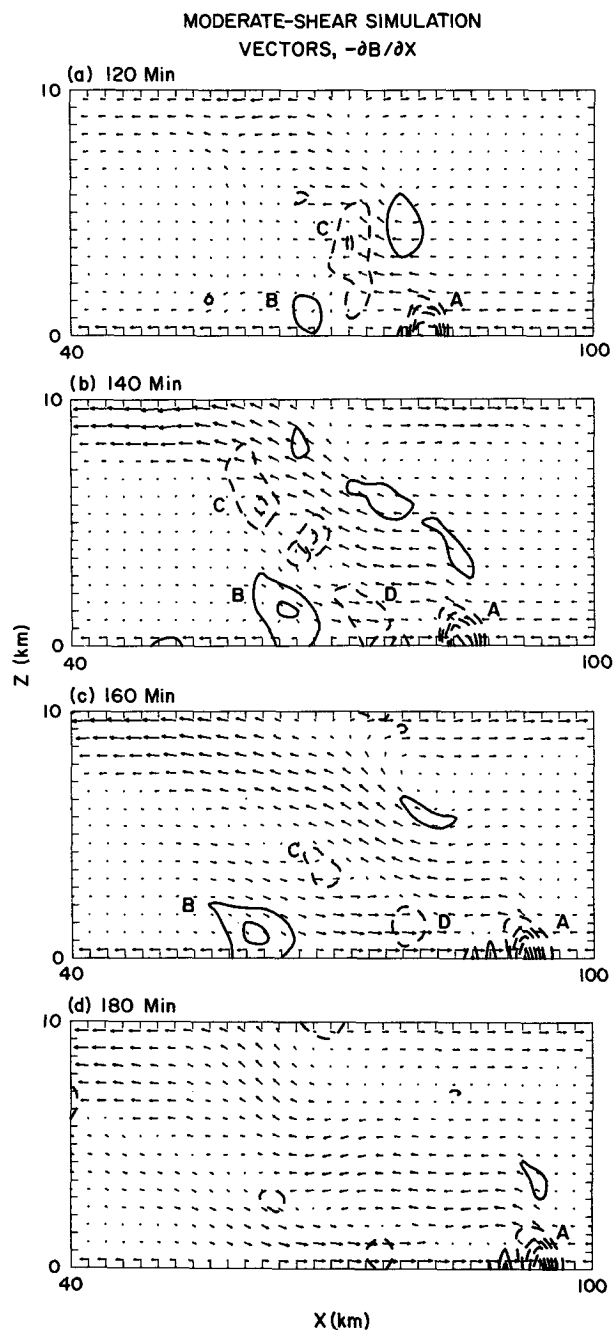
lated to the temperature excess within the rising parcels. For a conditionally unstable environment, the potential temperature excess realized by a surface parcel is usu-
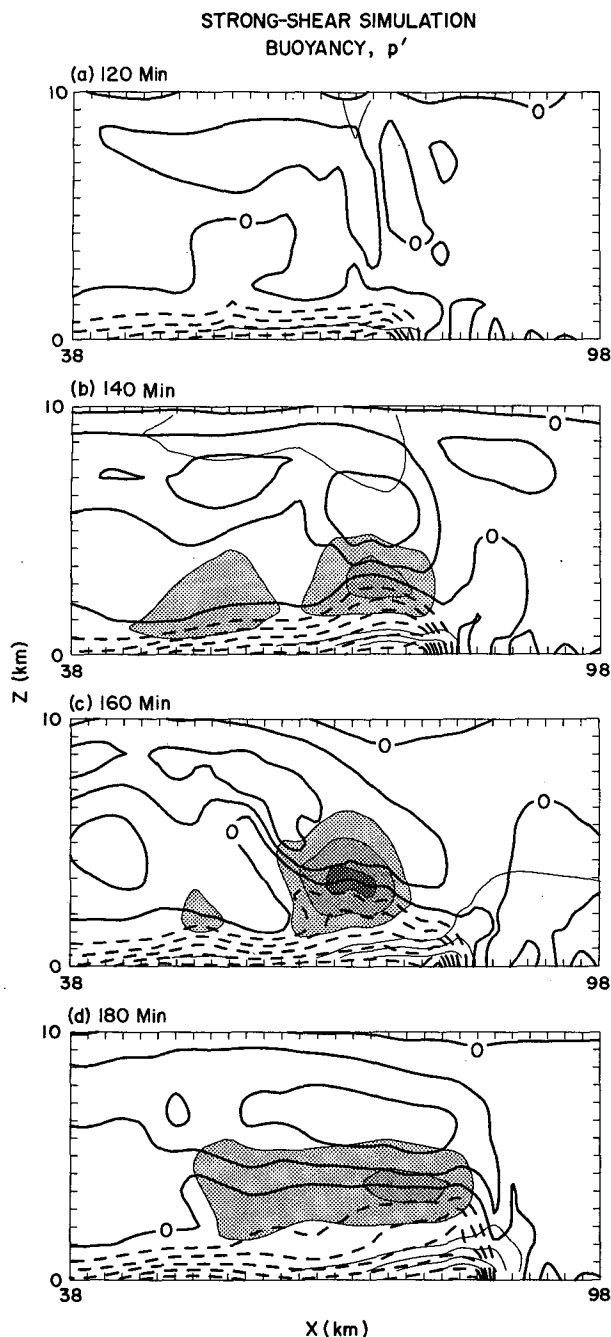
FIG. 11. As in Fig. 9 except for the strong-shear simulation.

FIG. 12. As in Fig. 10 except for the strong-shear simulation. A domain speed of $u = 22.5$ m s^{-1} is subtracted from the flow field.

ally maximized halfway through the troposphere, with the maximum magnitude of the temperature excess determined by the degree of instability within the sounding, as well as the amount of mixing experienced by the rising parcel. Thus, for a given thermodynamic profile, the maximum buoyancy is generally realized by surface parcels that are lifted to midtropospheric levels with a minimal amount of mixing within a tilted updraft.

The relative importance of these various contributions to updraft buoyancy for the moderate- and strong-

shear simulations has been analyzed by interpolating the perturbation potential temperature and water loading terms along the series of updraft trajectories presented in Figs. 13a and 14a. Each trajectory originates at 0.35 km AGL about 10 km ahead of the surface gust front at 120 min and is traced for an additional 60 min. This represents the time period of maximum rear-inflow generation for each case.

In both simulations, the updraft trajectories tilt rear-

MODERATE-SHEAR SIMULATION
$(U_s = 15 \, ms^{-1})$

a) Updraft Trajectories Beginning at 120 min

b) θ' (interpolated along trajectories)
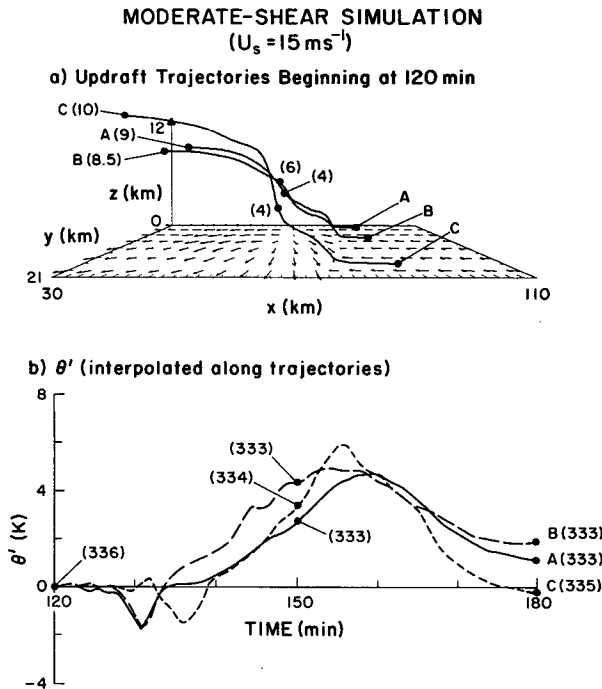

FIG. 13. (a) Characteristic updraft trajectories at 120 min for the moderate-shear simulation. Each trajectory originates at 350 m above the surface and about 10 km ahead of the cold pool at 120 min and is traced for an additional 60 min. The height of each trajectory is presented in parenthesis at 150 and 180 min. (b) A time series of the perturbation potential temperature as interpolated along each trajectory in (a). The value of θ_e as interpolated along each trajectory is presented in parentheses at 120, 150, and 180 min.

ward above the spreading cold pool as the air parcels are lifted to the upper troposphere. However, the slope of the trajectories for the strong-shear simulation is initially much steeper than for the moderate-shear case, with the maximum height attained by the strong-shear parcels generally 0.5–1 km higher than for the weaker shear case (9–11 km AGL versus 8.5–10 km AGL). This difference in trajectory slope is directly related to the relative balance between the cold pool and ambient vertical wind shear that is observed for each case (e.g., Fig. 8). For the moderate-shear simulation, the cold-pool circulation at 120 min is much stronger than that associated with the ambient shear ($C/\Delta u = 1.3$), and as such, the trajectories are drawn rapidly rearward above the leading edge of the cold air. For the strong-shear simulation, however, the cold-pool circulation is more closely matched to the ambient shear ($C/\Delta u = 0.9$), and the trajectories rise more vertically above the leading edge of the cold air.

As discussed above, the major contribution to the buoyancy within these tilted updrafts is the potential temperature perturbations created by the lifting process. A time series of the perturbation potential temperature as interpolated along each set of trajectories is presented in Figs. 13b and 14b, respectively. For reference, the maximum potential temperature excess that can be realized for a parcel lifted from near the

surface for the present sounding is 9.5 K, which occurs at a height between 7.0 and 7.5 km AGL. In both cases, the maximum potential temperature excesses are realized at 6.5 to 7.0 km AGL, with magnitudes ranging between 4.5 and 7.0 K. These values are significantly lower than the predictions of parcel theory, emphasizing the important role of mixing along the parcel's path in controlling the thermodynamic characteristics of the updraft current. However, even though both sets of trajectories lift surface parcels beyond the level of maximum buoyancy on the preconvective sounding, the maximum potential temperature perturbations associated with the strong-shear simulation average about 1.5 K larger than those for the moderate-shear case. This 1.5-K difference in the potential temperature perturbations translates to an $\sim 400 \, m^2 \, s^{-2}$ change in the magnitude of the full buoyancy, which is sufficient to explain the differences in the buoyancy fields presented in Figs. 10 and 12.

This suggests that the difference in potential temperature characteristics for the two sets of trajectories is due primarily to the amount of mixing experienced by the air parcels as they traverse to the midtroposphere. Indeed, an analysis of the equivalent potential temperatures interpolated along the trajectories (shown at 30-min intervals on Figs. 13b and 14b) does reveal an additional 2–3 K decrease in θ_e along the moderate-shear trajectories. This is also evident from the cross sections presented in Figs. 9 and 11, which reveal that the average equivalent potential temperature within the updraft current for the moderate-shear case is significantly less than that observed for the strong-shear
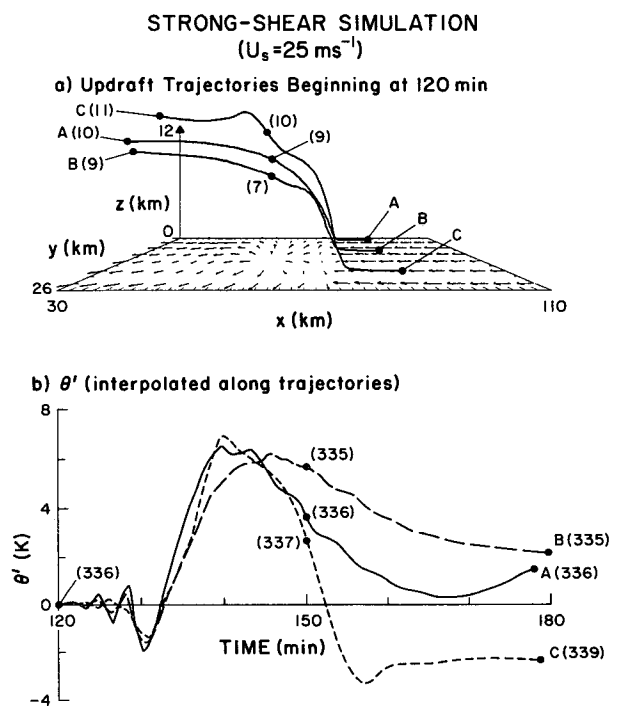
STRONG-SHEAR SIMULATION
$(U_s = 25 \, ms^{-1})$

a) Updraft Trajectories Beginning at 120 min

b) θ' (interpolated along trajectories)

FIG. 14. As in Fig. 13 except for the strong-shear simulation.

simulation. Much of this decrease in θ_e for the moderate-shear trajectories occurs during the early portion of the parcel ascent, as the surface parcels traverse along the top of the cold pool.

A similar analysis performed for the water loading terms (not shown) fails to reveal any significant variations between the two simulations, with water loading generally reducing the maximum buoyancy along the trajectories by about 20%. This suggests that the strong-shear simulation produces a warmer, more buoyant plume of air aloft due primarily to its tendency to lift the surface air more quickly, thus reducing the net mixing along the edge and top of the surface cold pool.
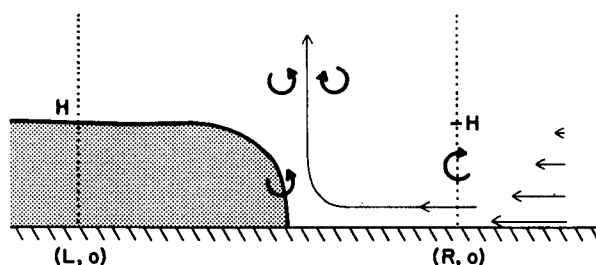
5. An extension to the RKW theory: The role of rear-inflow jets

Section 4 describes how rear-inflow will evolve in a convective system as the cold-pool circulation overwhelms the ambient shear, forcing the convective circulation to tilt upshear and weaken. For the moderate-shear simulation, the generation of midlevel rear-inflow that descends and spreads along the surface does not significantly alter this evolution. For the strong-shear simulation, however, the production of an elevated rear-inflow jet limits this process, and a strong, erect updraft circulation redevelops at the leading edge of the system. This structure is maintained despite a continuing imbalance between the cold-pool circulation and that associated with the ambient vertical wind shear. In developing their theory, RKW assumed that the flow within the cold pool is stagnant (relative to the motion of the leading edge of the cold air). This assumption was based on analyses performed during the early phase of the convective system, before significant rear-inflow features were generated. The present results suggest that this condition must be reexamined to include the effects of rear-inflow jets on the later evolution of such systems.
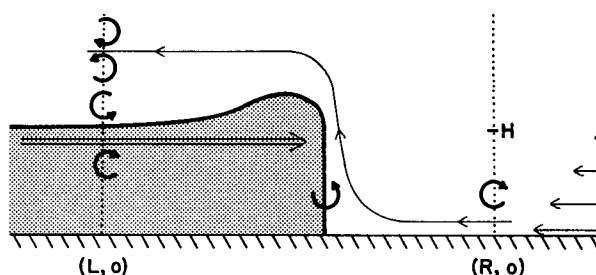
The effect of the rear inflow on the relative cold pool–shear balance can be visualized by considering the rear inflow as an additional source of horizontal vorticity that must be included in the balance condition. As a starting point, a schematic depicting a cold pool balanced by a vertically sheared environment is reproduced in Fig. 15a. In this scenario, the flow within the cold pool is assumed to be stagnant (relative to the leading edge of the cold air), and the only sources of horizontal vorticity are the vorticity associated with the ambient shear and the vorticity generated by the buoyancy gradients along the leading edge of the cold pool. With the vorticity sources equal in magnitude but opposite in sign, the low-level flow approaching the cold pool is turned vertically by the cold pool and exits the top of the domain.

The vertical circulation associated with an elevated rear-inflow jet is now represented schematically in Fig. 15b. In this case, a jet of air is placed near the top of the cold pool and remains at that height, H, until it

FIG. 15. Schematic depiction of (a) a cold pool spreading in an environment having sufficient vertical wind shear to balance the cold-pool-generated circulation, (b) a cold pool balanced by the ambient vertical wind shear and an elevated rear inflow jet, and (c) a cold pool in the presence of a surface rear-inflow jet. The shading denotes the region of negatively buoyant air. The thick arrows depict the sense of the vorticity that is generated at the leading edge of the cold pool or that is advected through the boundaries.

reaches the leading edge of the cold pool. This jet now represents a source of horizontal vorticity in addition to the vorticity associated with the ambient shear and generated by the cold pool. Below the level of maximum rear inflow, this vorticity is of the same sign as that of the ambient shear. Above this level, the vorticity is of the same sign as that generated by the cold pool. Thus, below jet level, the rear-inflow jet can act to counterbalance some of the horizontal vorticity produced by the cold pool. Since significant rear inflow is generated only after the cold-pool circulation overwhelms the ambient shear (forcing the system to tilt upshear), the elevated rear inflow contributes to reestablishing a balanced condition at the gust front, thereby producing stronger and deeper lifting at that location. Once the air is lifted above jet level, the vor-

ticity associated with the upper portion of the jet (which is of the same sign as that generated by the cold pool) then diverts the updraft current rearward.

A schematic representing the flow configuration for a rear-inflow jet that descends and spreads along the surface well behind the leading edge of the system is presented in Fig. 15c. As discussed above, the upper portion of this jet is characterized by the same sign of horizontal vorticity that is generated by the cold pool. Thus, the surface rear inflow acts to accentuate the upshear-tilting process already begun by the cold pool, thereby promoting even weaker and shallower lifting along the leading edge of the system.

These results may be established more quantitatively by formally rederiving the RKW vorticity-balance conditions for these more complicated flow scenarios. The derivation is based on an integration of the two-dimensional vorticity equation over an area encompassing the leading edge of the spreading cold pool. By accounting for all of the sources and sinks of vorticity within this specified control volume, solutions can be sought that represent the steady-state flow configurations described in the above examples. For this purpose, (3) is more conveniently written in flux form:

$$\frac{\partial \eta}{\partial t} = -\frac{\partial}{\partial x}(u\eta) - \frac{\partial}{\partial z}(w\eta) - \frac{\partial B}{\partial x}. \quad (4)$$

A coordinate system is chosen that moves at the speed of the propagating cold pool, and the vorticity equation is integrated over a box centered on the cold-pool edge. The original derivation extends this control volume to an arbitrary height, d, above the top of the cold pool, but, for the present purposes, it is most convenient to limit the top of the control volume to the height of the cold pool, H. This yields the following integral equation:

$$\underbrace{\frac{\partial}{\partial t} \int_L^R \int_0^H \eta \, dz \, dx}_{\text{tendency}}$$

$$= \underbrace{\int_0^H (u\eta)_L \, dz}_{\text{flux at left}} - \underbrace{\int_0^H (u\eta)_R \, dz}_{\text{flux at right}}$$

$$- \underbrace{\int_L^R (w\eta)_H \, dx}_{\text{flux at top}} + \underbrace{\int_0^H (B_L - B_R) \, dz}_{\text{net generation}}, \quad (5)$$

where it is assumed that $w = 0$ at the surface. Since a steady solution is sought, the tendency term is set to zero. Also, it is assumed that the buoyancy of the ambient air approaching the cold pool from the right is negligible, and thus B_R is set to zero. Finally, η is approximated as $\partial u/\partial z$ away from the edge of the cold air. Under these conditions, (5) may be rewritten as

$$0 = \left(\frac{u_{L,H}^2}{2} - \frac{u_{L,0}^2}{2}\right) - \left(\frac{u_{R,H}^2}{2} - \frac{u_{R,0}^2}{2}\right)$$

$$- \int_L^R (w\eta)_H \, dx + \int_0^H B_L \, dz. \quad (6)$$

If the cold air is assumed to be stagnant (relative to the cold air edge), then both $u_{L,0} = 0$ and $u_{L,H} = 0$. It is this condition of zero flow within the cold pool that must be modified to explain the effects of the rear inflow. For now, (6) becomes

$$0 = -\left(\frac{u_{R,H}^2}{2} - \frac{u_{R,0}^2}{2}\right) - \int_L^R (w\eta)_H \, dx + \int_0^H B_L \, dz. \quad (7)$$

If a balanced state is sought such that the ambient low-level flow is turned vertically by the cold pool and exits above the cold pool as a symmetric, vertically oriented jet, then the integral of $w\eta$ across the jet may be set to zero. Also, if the jet is to continue traveling vertically above the height of the cold pool, H, as depicted in Fig. 15a, then we require zero ambient shear and zero ambient flow relative to the cold-pool edge in the environment above H. This requires that $u_{R,H} = 0$, yielding the expression

$$\Delta u^2 = C^2, \quad \text{where} \quad \Delta u^2 \equiv u_{R,0}^2, \quad (8)$$

and where C is given by (1). This represents the "optimal" state of RKW, whereby the import of the positive vorticity associated with the low-level shear just balances the net buoyant generation of negative vorticity by the cold pool in the volume. As discussed earlier, the degree of balance can be expressed conveniently in terms of the ratio $C/\Delta u$, where a ratio of 1 represents the optimal condition.

In order to account for the influence of a rear-inflow, we retain the terms in (6) as before, but now consider the possibility of relative flow within the cold pool by including the first term on the rhs of (6). Again, if a balanced state is sought such that the flow exits above the cold pool as a vertically oriented jet, then

$$\Delta u^2 = C^2 - \Delta u_J^2 \equiv C_J^2 \quad \text{where} \quad \Delta u_J^2 \equiv u_{L,H}^2 - u_{L,0}^2. \quad (9)$$

This expression now represents the relative balance between the generation of negative vorticity by the cold-pool edge and the flux of horizontal vorticity through both the right and left boundaries, associated with the ambient vertical wind shear and the rear-inflow jet, respectively (note that Δu_J^2 may be less than zero). For the simple scenario of an elevated jet with $u_{L,0} = 0$, Δu_J^2 represents a net flux of positive horizontal vorticity through the left boundary of the control volume and thus contributes toward balancing the circulation generated by the cold pool. This proposed flow configuration is very close to that depicted in Figs. 6c,d for the strong-shear simulation. However, if a rear-inflow jet spreads along the surface, with $u_{L,0} > u_{L,H}$, then Δu_J^2 represents a net flux of negative horizontal vorticity through the left boundary of the control volume and contributes in the same sense as the cold pool. This proposed flow configuration is closer to that depicted in Figs. 4c,d for the moderate-shear simulation, where

the magnitude of $u_{L,0}$ is much greater than the magnitude of $u_{L,H}$.

These results can be made more quantitative by explicitly calculating the terms included in (9) for the moderate- and strong-shear simulations. For this purpose, the terms representing conditions within the cold pool are calculated as averages of each quantity within 10 km of the cold-pool edge. Also, a frame of reference is chosen such that $u_{R,H} = 0$, so that Δu remains constant for each case and always represents the magnitude of the ambient low-level vertical wind shear. When a balanced state exists such that $C_J/\Delta u = 1$, this frame of reference also represents one that moves with the gust front, as specified in the derivations above. Departures from this balanced state also represent departures from the proposed flow configuration of a steady, vertically oriented jet above the leading edge of the cold pool. Thus, the implied relationship between the gust-front speed and the ambient midlevel flow would also no longer hold.

Figure 16 presents a time series of $C_J/\Delta u$ for the moderate- and strong-shear simulations. In both cases, the rear-inflow accelerates significantly between 120 and 180 min when the updraft circulations are tilting upshear ($C/\Delta u$ is already greater than 1; see Fig. 8). For the moderate-shear case, the rear inflow descends and spreads along the surface, and $C_J/\Delta u$ increases from 1.3 at 120 min, prior to any significant rear inflow, to 2.0 once the jet is established. Thus, the role of the jet is to bring the system further from the optimal condition of $C_J/\Delta u = 1$. Consistent with this, the system circulation remains shallow through 240 min.

For the strong-shear simulation, the cold pool continues to strengthen after 120 min and $C/\Delta u$ increases to 1.4 (Fig. 8). Based on the RKW theory alone, we would expect the circulation at the leading edge of the system to continue to tilt upshear and become shallower. However, with the elevated rear inflow included in the new balance expression, $C_J/\Delta u$ decreases to 1.2, which is closer to the optimal condition of $C_J/\Delta u = 1$, and a quasi-steady, vertically oriented updraft is maintained at the leading edge of the gust front.
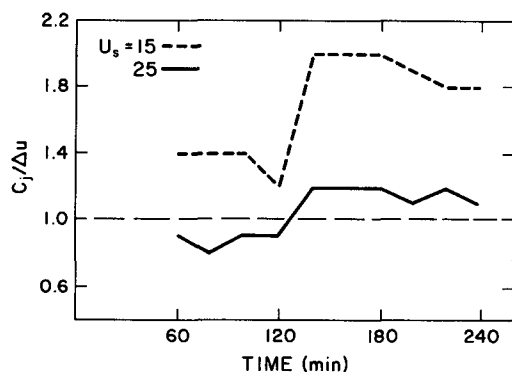
Thus, the inclusion of the rear-inflow jet in the cold pool–vertical shear balance conditions of RKW leads to a more complete and consistent picture of the evolution of these simulated convective systems. However, we note that for strengths of the cold pools produced in these simulations, Δu_J^2 must reach magnitudes > 100 m^2 s^{-2} (i.e., rear inflow strengths > 10 m s^{-1}) to have a significant impact on the $C/\Delta u$ criteria originally proposed by RKW. Since Smull and Houze (1987) document that only a small percentage of their cases displayed rear inflows of such large magnitude, it may be that the RKW theory alone (without the addition of the rear-inflow current) may still be sufficient to characterize the evolution of most observed convective systems.

6. Environmental controls on rear-inflow strength and structure

The analyses of the preceding sections suggest that the strength and structure of convectively generated rear-inflow jets depend on the characteristics of both the low-level vertical wind shear and the thermodynamic profile in the environment ahead of the system. The vertical wind shear modulates the characteristics of the lifting that can be realized at the leading edge of the gust front, thus controlling the amount of buoyancy realized in the warm plume spreading aloft as well as the strength of the cold pool at the surface (i.e., stronger convection aloft tends to produce stronger downdrafts and stronger cold pools). The thermodynamic profile, on the other hand, ultimately controls the maximum amount of buoyant energy that can be realized by a given amount of lifting as well as the maximum amount of cooling that can be realized in the downdrafts. The discussion so far has concentrated on the analysis of simulations using a single thermodynamic profile, with the wind shear restricted to the lowest 2.5 km AGL. The goal of this section is to document the sensitivity of these results to variations in both of these sets of conditions.

In order to accomplish this, key rear-inflow jet characteristics have been tabulated for the entire range of buoyancy and shear conditions specified in section 2. We will especially emphasize the attributes of the rear-inflow jets that address the dynamics issues discussed in the previous sections. In particular, we are interested in both the strength of the midlevel current that is generated within the rearward-expanding system as well as its elevation as it approaches the leading edge of the system. In addition, we have made an effort to consider only those rear-inflow jets that represent a quasi–two-dimensional mesoscale response to the convective activity, as opposed to more localized features associated with individual convective cells. Such localized wind maxima are especially evident in the stronger, deeper-shear experiments where isolated, three-dimensional supercells are the dominant convective structures. These specific cases have been eliminated from the analysis.

FIG. 16. Time series of $C_J/\Delta u$ for the moderate- (dotted line) and strong-shear (solid line) simulations.

We present specifically results representing the average structure of the convective systems between 200 and 240 min, after the rear-inflow circulations have become well established. The strength of the jet is defined as the maximum magnitude of the rear-inflow current observed between 2- and 4-km AGL and within 8 to 40 km of the leading edge of the cold pool. The elevation of the jet is defined as the height of the maximum rear-inflow at a location of 8 km behind the leading edge of the cold pool. For consistency, all measurements are made on the symmetry axis of the simulations.

There are several plausible frameworks that can be used to present the strength of the jet, that is, relative to cell motion, relative to gust-front motion, relative to the ambient winds at a given height AGL, etc. Since there does not appear to be a dynamically unique choice, we offer the reader two options to aid in their interpretation. First, to emphasize the ability of the convective system to accelerate the ambient flow, we present the strength of the jet relative to the ambient 2.5-km flow, which is the maximum ground-relative wind in the preconvective environment. Second, since the air in the rear-inflow current must be moving faster than the convective system to have a significant impact on its dynamics, we also present the strength of the rear inflow relative to system motion, which for our purposes is defined to be the motion of the gust front. This latter reference frame is also the one most often used in previous observational studies.

The previous sections also stress the dependence of rear-inflow strength and structure on the strength of the horizontal buoyancy gradients that are produced by the convective circulations. In order to demonstrate this relationship more clearly, we present the maximum buoyancy perturbations observed aloft and at the surface for each simulation, as measured between 8 and 40 km behind the leading edge of the gust front and averaged between 200 and 240 min. These maximum buoyancy perturbations serve as a simple, useful measure of the existing horizontal buoyancy gradients, although one still needs to know the detailed variations to the buoyancy field for explicit calculations. Since this analysis encompasses a period when the systems have already developed a mature, quasi-steady structure, the correlation between the buoyancy perturbations and rear-inflow strength does not necessarily support cause and effect relationships. However, the previous analysis of section 4 clearly shows how the rear inflow is generated in response to the horizontal buoyancy gradients (and associated horizontal pressure gradients) rather than vice versa.

Finally, since it is often difficult to estimate the contributions to the full buoyancy field from the water-loading terms for observational datasets, we also present the average maximum potential temperature perturbations observed aloft and at the surface between 200 and 240 min for these simulations. In general, we find that the potential temperature perturbations explain over 75% of the buoyancy perturbations in the regions not dominated by intense convective cells.

a. Shallow-shear simulations

Figure 17 presents the maximum magnitude of the rear inflow observed for the 2.5-km shear simulations, with the cases that produce elevated jets denoted by the shaded regions. Cases in which the convective system does not survive through 240 min are indicated by 0's, while cases in which isolated supercells are the dominant convective mode are indicated by an "S." In general, the strength of the rear inflow increases steadily for both increasing CAPE and increasing vertical wind shear, with the rear-inflow jets remaining elevated for shear magnitudes of $U_s > 15$ m s^{-1}. From the 2.5-km-relative perspective (Fig. 17a), rear inflow jets > 10 m s^{-1} are generated for almost all of the cases with a CAPE greater than 1700 m^2 s^{-2}. However, from

MAXIMUM MID-LEVEL REAR INFLOW
(2.5 km Shear Simulations)

FIG. 17. Average maximum magnitude of the midlevel rear inflow (m s^{-1}) observed for the 2.5-km shear simulations between 200 and 240 min, presented (a) relative to the ambient 2.5-km flow and (b) relative to the motion of the gust front, as described in the text. U_s represents the maximum magnitude of the ambient wind for the wind profile, as described in section 2. The shaded region depicts the cases that produced elevated rear-inflow jets.

the system-relative perspective (Fig. 17b), rear inflow > 10 m s^{-1} occurs over a more restricted range of CAPEs (>2400 m^2 s^{-2}) and vertical wind shears (U_s > 15 m s^{-1}). These also represent the cases in which the rear inflow remains elevated.

As with the rear-inflow strength, Fig. 18 also depicts a systematic increase in the magnitude of the buoyancy perturbations observed aloft and at the surface for increasing CAPE and ambient vertical wind shear. For a given value of CAPE, the positive buoyancy excesses aloft increase by over 100% over the range of shears simulated. The buoyancy deficits at the surface, however, do not increase as dramatically over the shear range. This leads to a higher ratio of buoyancy excess aloft to buoyancy deficit at the surface for increasing shear. For the present simulations, a magnitude of $B_{max}/|B_{min}| > 0.5$ seems consistent with the development of the elevated jets. This is qualitatively consistent with the hypothesis that relatively strong buoyancy gradients aloft are necessary for the production

MAXIMUM BUOYANCY PERTURBATIONS
(2.5 km Shear Simulations)

(a) Maximum Buoyancy Aloft

(b) Minimum Buoyancy at the Surface

VERTICAL WIND SHEAR(Us) (ms^{-1})

FIG. 18. Average maximum magnitude of the buoyancy perturbations (10^{-3} m s^{-2}) observed (a) aloft and (b) at the surface for the 2.5-km shear simulations between 200 and 240 min, as described in the text. U_s represents the maximum magnitude of the ambient wind for the wind profile, as described in section 2. The shaded region depicts the cases that produced elevated rear-inflow jets.

of the elevated jets. The average potential temperature perturbations (Fig. 19) display a similar dependence on CAPE and vertical wind shear as the buoyancy perturbations do, demonstrating the potential for this single parameter in characterizing qualitatively the full buoyancy field.

b. Deep-shear simulations

The generation of rear-inflow in the 5-km shear simulations is more difficult to interpret as shear strengths sufficient to ensure long-lived convective systems are also more conducive to development of isolated, three-dimensional supercells (e.g., Weisman et al. 1988). Also, with the deeper shears, it is more difficult to choose a reference height that can be used to discern how much of the rear inflow is generated by the convective system versus how much represents ambient flow. With the rear-inflow jets for these deeper-shear simulations generally located below 4 km AGL, part of the observed rear-inflow strength could be due to the downward transport of momentum from levels where the ambient winds are stronger. However, for consistency with the previous results, we will continue to present the rear-inflow strengths at midlevels relative to the ambient 2.5-km flow.

The results are generally consistent with the 2.5-km shear simulations, with the magnitude of the rear inflow increasing for both increasing shear and increasing CAPE. As transformed in the system-relative framework (Fig. 20b), however, significant rear inflow is even more restricted to higher shears and higher CAPEs than for the shallow-shear simulations. The buoyancy perturbations (Fig. 21) and potential temperature perturbations (Fig. 22) also show a dependence similar to the 2.5-km shear simulations, but the range of variation for the positive perturbations is not quite as large as for the shallower-shear simulations.

c. Comparison with previous numerical simulations and observations

A comparison of the present results with those derived from the recent two-dimensional simulations noted in the Introduction reveals many similarities. For instance, Fovell and Ogura (1989) and Lafore and Moncrieff (1989) both document an increase in rear-inflow strength with increasing magnitude of the ambient vertical wind shear, with Lafore and Moncrieff also noting an increase in rear-inflow strength with increasing CAPE. In addition, the Fovell and Ogura simulations clearly display a tendency for the rear-inflow jet to be more elevated for stronger shears. These stronger, more elevated rear inflows are also associated with larger potential temperature perturbations aloft and at the surface, as described in the present simulations.

While the comparisons between the present results and past numerical studies are quite favorable, similar
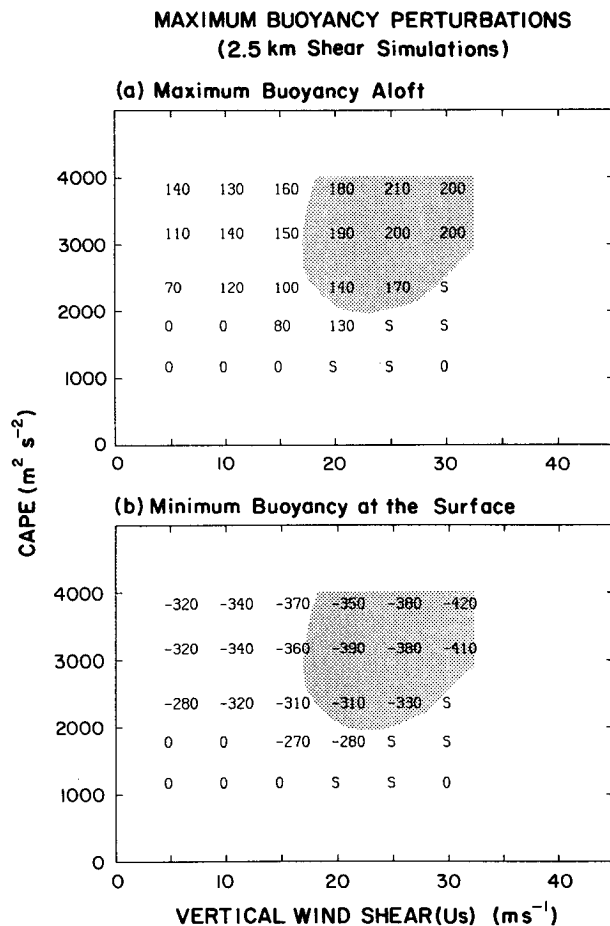
MAXIMUM POTENTIAL TEMPERATURE PERTURBATIONS
(2.5 km Shear Simulations)

(a) Maximum θ' Aloft

(b) Minimum θ' at the Surface

VERTICAL WIND SHEAR (Us) (ms^{-1})

FIG. 19. Average maximum magnitude of the potential temperature perturbations (K) observed (a) aloft and (b) at the surface for the 2.5-km shear simulations between 200 and 240 min, as described in the text. U_s represents the maximum magnitude of the ambient wind for the wind profile, as described in section 2. The shaded region depicts the cases that produced elevated rear-inflow jets.
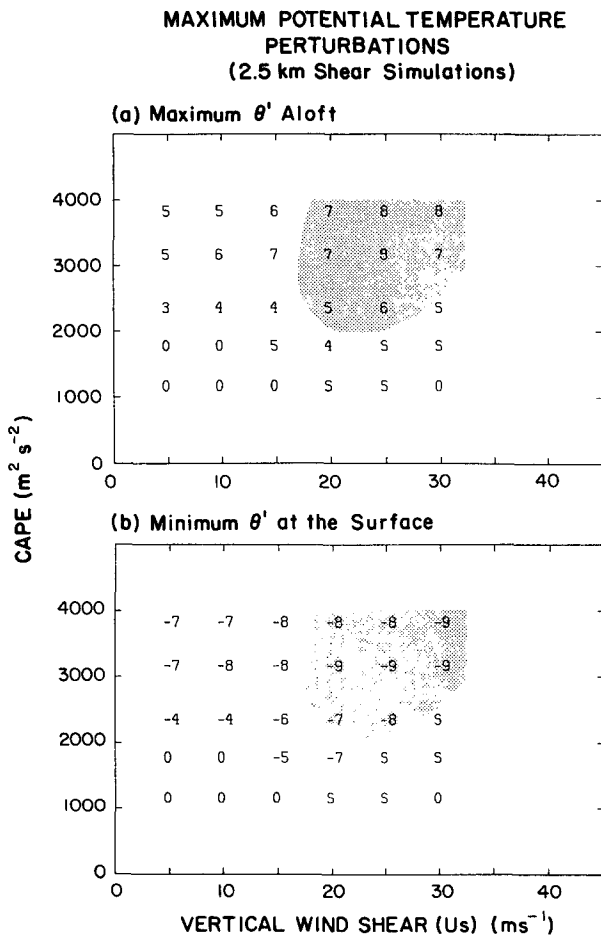
comparisons with observed cases are more difficult to interpret. Observed rear-inflow jets are often the product of both the internal generation mechanisms discussed above as well as the natural horizontal variability in the preconvective winds. In addition, there is also often much horizontal variability in the environmental CAPE and vertical wind shear conditions ahead of the convective system, making it difficult to characterize the environmental controls on the evolution of the convection. No attempt has been made for this preliminary discussion to distinguish among the various sources for the observed rear-inflow jets, nor has there been a careful review of the evolution of the environments in the vicinity of the convective systems. This essential task will await a future study. Still, certain similarities between the present results and observational studies are worthy of note.

In general, most observed cases are characterized by rear-inflow jets that descend and spread along the surface well behind the leading edge of the system. Notable

examples of this structure include the 22 May 1976 case [described by Ogura and Liou (1980) and Smull and Houze (1987) and also simulated by Fovell and Ogura (1988)] and the 10–11 June 1985 case [described by Smull and Houze (1987) and Rutledge et al. (1988), as well as many other authors]. Both of these systems developed in environments of moderate CAPE (2000–3000 m^2 s^{-2}) with the component of vertical wind shear perpendicular to the squall line ranging from $U_s = 10$ to 15 m s^{-1} over the lowest several kilometers AGL. The rear inflow for the 22 May case descended to the surface nearly 100 km behind the leading edge of the system, with a strength at midlevels of up to 10 m s^{-1} (relative to system motion) at the far back edge. The rear-inflow for the 10–11 June case evolved over several hours, remaining elevated to near the leading edge of the active convective zone at early times but then descending and reaching the surface about 30 km behind the leading edge of the system at later times (e.g., Rutledge et al. 1988). The strength of the midlevel rear inflow for this case ranged from about 10 m s^{-1} at a distance of 50 km to over 15 m s^{-1} at a distance of 150 km behind the system's leading edge. Consistent with the results presented in Figs. 17 and 20, both of these cases were observed to be declin-

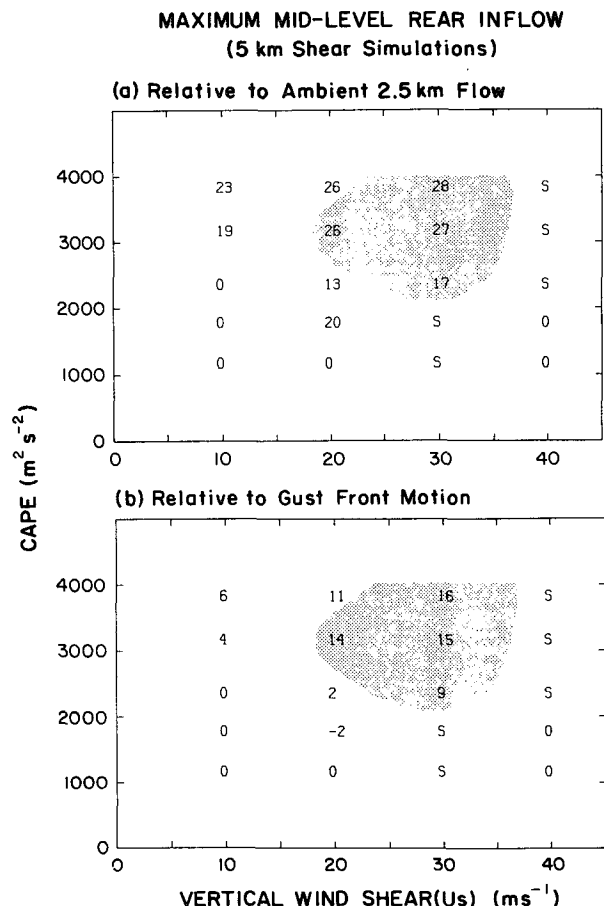## MAXIMUM MID-LEVEL REAR INFLOW
(5 km Shear Simulations)

(a) Relative to Ambient 2.5 km Flow

(b) Relative to Gust Front Motion

VERTICAL WIND SHEAR(Us) (ms^{-1})

FIG. 20. As in Fig. 17 except for the 5.0-km shear simulations.

MAXIMUM BUOYANCY PERTURBATIONS
(5 km Shear Simulations)

(a) Maximum Buoyancy Aloft

(b) Minimum Buoyancy at the Surface

VERTICAL WIND SHEAR(Us) (ms⁻¹)

Fig. 21. As in Fig. 18 except for the 5.0-km shear simulations.

ing in strength as the rear-inflow descended and spread along the surface.

The 28 May 1985 case described by Smull and Houze (1987) and the 22 June 1981 case described by Chong et al. (1987) displayed more elevated rear-inflow jet structures, with the strength of the system-relative midlevel rear inflow ranging between 10 and 15 m s⁻¹ within 20 km of the system's leading edge. The CAPE for the 22 June case was less than that reported for the above cases (1300 m² s⁻²), but the vertical wind shear was stronger (15 to 20 m s⁻¹ over the lowest several kilometers AGL). An analysis of the environment of the 28 May case has not yet been completed. Both of these cases also displayed much variation in rear-inflow structure along the convective line, suggesting that three-dimensional influences may be more important in understanding the evolution of these types of systems. However, in some agreement with the present simulations, both of these more elevated jet cases were associated with convective systems that maintained their strength for many hours after the onset of the rear-inflow circulation.

The strongest, most elevated convectively generated rear-inflow jets may be observed with mesoconvective structures referred to as "bow echoes." These long-lived

convective events are well known to produce long swaths of damaging surface winds (e.g., Fujita 1978). Doppler radar analysis of a bow echo observed in Oklahoma by Burgess and Smull (1990) suggests that the system-relative rear-inflow strengths in such events may reach magnitudes of 25 m s⁻¹. Climatological studies by Johns and Hirt (1987) and Johns et al. (1990) suggest that these systems tend to evolve in environments of extreme instability (CAPEs of over 3000 m² s⁻²) and strong low-level vertical wind shear (U_s > 15 m s⁻¹ over the lowest several kilometers AGL). These are also the environmental conditions associated with the strongest, most elevated rear-inflow jets in the above simulations. These structures are discussed more completely in a companion paper by Weisman (1992).

7. Summary and discussion

In the foregoing, convective systems were simulated for a wide range of ambient vertical wind shears and CAPEs for the purpose of better understanding the mechanisms that control the generation of midlevel rear-inflow jets as well as understanding the influence

MAXIMUM POTENTIAL TEMPERATURE
PERTURBATIONS
(5 km Shear Simulations)

(a) Maximum θ' Aloft

(b) Minimum θ' at the Surface

VERTICAL WIND SHEAR(Us) (ms⁻¹)

Fig. 22. As in Fig. 19 except for the 5.0-km shear simulations.

these jets have on the subsequent evolution of the convective systems. As represented schematically in Fig. 2, rear inflow is generated in these simulations in response to the development of an upshear-tilted updraft, as the horizontal buoyancy gradients along the back edge of the expanding system create a circulation that draws midlevel air in from the rear. The influence of the rear inflow on the subsequent evolution of the convective system, however, varies considerably depending on the structure and strength of this rear-inflow current.

The range of mature convective structures that are realized in these simulations once a rear-inflow jet becomes established is represented schematically in Fig. 23, which depicts idealized convective systems characterized by rear-inflow jets that either remain elevated to near the leading edge of the system or descend and spread along the surface well behind the leading edge of the system. For a descending-jet system (Fig. 23a), the convective circulation is characterized by an updraft current that ascends gradually above a spreading surface cold pool, with light-to-moderate convective and

(a) Descending Rear-Inflow

(b) Elevated Rear-Inflow

FIG. 23. A conceptual model of the mature structure of a long-lived squall-line–type convective system for (a) a system with a descending rear-inflow jet and (b) a system with an elevated rear-inflow jet. The updraft current is denoted by the thick, double-lined flow vector, while the rear-inflow current is denoted by the thick, dashed flow vector. The shading denotes the surface cold pool. The thin, circular arrows depict the most significant sources of horizontal vorticity, which are either associated with the ambient shear or which are generated within the convective system, as described in the text. Regions of lighter or heavier rainfall are indicated by the more sparsely or densely packed vertical lines, respectively. The scalloped line denotes the outline of the cloud.

stratiform rainfall extending well behind the leading edge of the cold pool. This structure is often associated with a decaying system, whereby the gust-front lifting is not strong or deep enough to regenerate new convective cells and the mesoscale circulation slowly weakens. For an elevated-jet system (Fig. 23b), however, the circulation is dominated by strong, erect updrafts along the leading edge of the surface cold pool, with the updraft current spreading rapidly rearward above 7–8 km AGL. Moderate-to-heavy convective rainfall exists at the leading edge of the system, with lighter rainfall extending to the rear. This structure tends to be longer-lived than the descending-jet case, as strong convective cells are regularly regenerated by the deeper gust-front lifting.

The apparently distinct roles of the rear-inflow jets in the evolution of these convective systems has been analyzed within the context of the recent theory of RKW, who propose an "optimal" condition for the production of strong, deep updrafts along the leading edge of a spreading cold pool based on a balance between the horizontal vorticity generated by the cold pool and the horizontal vorticity inherent in the ambient vertical shear. Within this context, the rear-inflow jet represents a new, potentially significant source of horizontal vorticity that must be included when diagnosing the relative importance of the various sources of circulation. Specifically, a rear-inflow jet that descends and spreads along the surface is characterized by the same sign of horizontal vorticity as that generated by the cold pool, thereby accentuating the cold-pool circulation. In contrast, an elevated rear-inflow jet is characterized by the opposite sign of horizontal vorticity as that generated by the cold pool (up to jet level), thereby accentuating the effects of the ambient vertical shear. Since significant rear-inflow characteristically develops only after the cold-pool circulation overwhelms the ambient shear, the development of a surface jet accentuates the upshear-tilting process that tends to weaken the system. However, the development of an elevated rear-inflow jet reverses this process, promoting the regeneration of strong, upright convective cells along the leading edge of the cold pool.

Similar to RKW, the relative balance between the various sources of circulation can be expressed conveniently in the form of a ratio, $C_J/\Delta u$, where C_J represents the strength of the cold-pool circulation, now including the effects of the rear-inflow jet, and Δu represents the strength of the low-level ambient vertical wind shear. As before, a ratio of 1 represents the optimal condition for the production of strong, erect updrafts along the leading edge of the system. However, for the strengths of the cold pools produced in these simulations, rear-inflow jets of greater than 10 m s^{-1} must be generated to have a significant impact on the $C/\Delta u$ balance condition originally proposed by RKW.

The strength and structure of these rear-inflow jets is controlled by the magnitude of the horizontal buoyancy gradients that are produced along the back edge
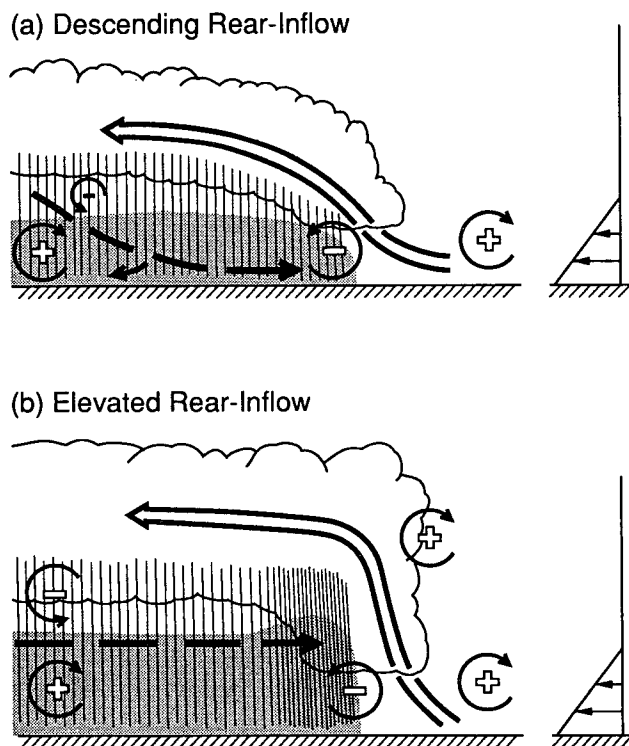
of the rearward-expanding convective system. In general, the rear-inflow strength increases for both increasing CAPE and increasing vertical wind shear. The CAPE controls directly the maximum amount of buoyancy that can be realized by a parcel lifted from near the surface, while the vertical wind shear controls the characteristics of the lifting produced near the leading edge of the system, thereby controlling the magnitude of the buoyancy perturbations that are actually realized both aloft and within the cold pool. The production of an elevated-versus-descending jet depends additionally on the relative strength of the horizontal buoyancy gradients along the back edge of the rearward-expanding system. If the horizontal buoyancy gradients associated with the warm plume aloft are equal or greater in magnitude than the horizontal buoyancy gradients associated with the cold pool near the surface, then the jet tends to remain elevated. However, if the cold-pool gradients are stronger than those aloft, then the jet descends and spreads along the surface.

The previous hypotheses concerning the role of rear-inflow jets in the evolution and maintenance of convective systems have emphasized either the impact that the dry current of air may have on the production of stronger downdrafts and cold pools (e.g., Fovell and Ogura 1989; Fovell 1991) or the impact that the rear-inflow momentum may have on enhancing the lifting along the leading edge of the cold pool (Smull and Houze 1987; Lafore and Moncrieff 1989). The present results emphasize how complicated these feedbacks may be. For instance, the strongest, most elevated rear-inflow jets in these simulations are also associated with the strongest and deepest cold pools. Thus, while the stronger cold pools may act to tilt the convective circulation rearward, the horizontal vorticity associated with the elevated jet may act to make the convective circulation more upright, etc. This makes it very difficult to gauge the net effect of the rear inflow on the convective circulation, a priori. The advantage of the present approach is that both of these effects have been incorporated into a single theory and are quantified via the ratio $C_J/\Delta u$. Thus, the relative importance of each effect can, in principle, be measured directly. In particular, for the present simulations, the primary influence of the rear-inflow jet appears to be through its transport of horizontal vorticity to the leading edge of the system, rather than through its influence on the strength of the cold pool. This hypothesis can now be tested for observational cases as well as additional simulations.

One of the possible limitations to the present results is the lack of ice processes in the model microphysics. Fovell and Ogura (1988) noted that the inclusion of ice in two-dimensional squall-line simulations enhanced the rearward flux of precipitation particles into the trailing portions of the storm, helping to produce a more extensive and realistic stratiform precipitation region. The melting of ice particles also contributed to increasing the coldness and depth of the subcloud cold pool, leading to a faster propagation speed for the system. Another possible influence of the ice would be to enhance the positive potential temperature perturbations aloft due to the latent heat of fusion. As suggested by Lafore and Moncrieff (1989), the primary impact of these processes is to change the distribution of the buoyancy field throughout the convective system, thereby modulating the intensity and structure of the generated circulations, including the rear-inflow jet. Future three-dimensional studies will need to establish more clearly the relative importance of these processes compared to the environmental factors discussed above in controlling the evolution of such convective systems.

Another possible concern is the lack of the Coriolis force in these simulations. Fovell (1991) found that the inclusion of the Coriolis force produced a "braking effect" on the rear inflow current for long-term (greater than 10 h) two-dimensional simulations, whereby the perturbed line-normal flow was turned to the right by the Coriolis accelerations. However, these two-dimensional simulations suggest that this effect is not significant for the shorter-term (4 h) simulations discussed herein.

The properties of convectively generated rear-inflow jets are investigated herein for very simple environmental conditions. Observed rear-inflow jets, however, evolve in much more complicated environments and are often the result of large-scale variations to the environmental winds as well as the internal processes discussed above. Although a cursory comparison between the present results and observations reveals general similarities, a much more careful evaluation is needed. Ideally, this should be accomplished by observing and analyzing the complete lifecycle of convective systems rather than concentrating just on the mature stage after the rear-inflow circulations have already been established.

In addition, both the modeling and observational studies suggest that the rear-inflow properties may vary considerably within a convective system, suggesting that three-dimensional influences may also need to be more carefully considered when analyzing the evolution of these features. The present simulations suggest that this may be especially true for stronger-shear environments, whereby midlevel vortices are observed to form at the ends of the convective system. Future studies must also consider how these midlevel vortices are related to the development of a larger cyclonic mesoscale vortex that has been observed later in the lifecycle of certain mesoscale convective systems (e.g., Zhang and Fritsch 1988). Preliminary results indeed suggest that if the Coriolis force is included, the original cyclonic midlevel vortex at the northern end of the simulated systems predominates over the southern anticyclonic vortex for integrations > 6 h, similar to the observations.

Finally, future studies must also systematically consider other variations to the convective environment, such as deeper shear profiles and multidirectional shear profiles, as well as variations to the vertical profile of moisture. It is hoped, however, that the present results will form a basis from which to interpret the effects of these more complicated environmental conditions on mesoscale-convective systems.

REFERENCES

Burgess, D. W., and B. F. Smull, 1990: Doppler radar observations of a bow echo associated with a long-track severe windstorm. Preprints, *16th Conf. on Severe Local Storms,* Kananaskis, Amer. Meteor. Soc., 203–208.

Chong, M., P. Amayenc, G. Scialom, and J. Testud, 1987: A tropical squall line observed during the COPT 81 experiment in West Africa. Part 1: Kinematic structure inferred from dual-Doppler radar data. *Mon. Wea. Rev.,* **115,** 670–694.

Fovell, R. G., 1991: Influence of the Coriolis force on two-dimensional model storms. *Mon. Wea. Rev.,* **119,** 606–630.

——, and Y. Ogura, 1988: Numerical simulation of a midlatitude squall line in two dimensions. *J. Atmos. Sci.,* **45,** 3846–3879.

——, and ——, 1989: Effect of vertical wind shear on numerically simulated multicell storm structure. *J. Atmos. Sci.,* **46,** 3144–3176.

Fujita, T. T., 1978: *Manual of Downburst Identification for Project Nimrod.* Satellite and Mesometeorology Research Paper No. 156, Dept. of Geophysical Sciences, University of Chicago, 104 pp.

Houze, R. A., 1977: Structure and dynamics of a tropical squall-line system. *Mon. Wea. Rev.,* **105,** 1540–1567.

——, S. A. Rutledge, M. I. Biggerstaff, and B. F. Smull, 1989: Interpretation of Doppler weather radar displays of midlatitude mesoscale convective systems. *Bull. Amer. Meteor. Soc.,* **70,** 608–619.

——, B. F. Smull, and P. Dodge, 1990: Mesoscale organization of springtime rainstorms in Oklahoma. *Mon. Wea. Rev.,* **118,** 613–654.

Johns, R. H., and W. D. Hirt, 1987: Derechos: Widespread convectively induced windstorms. *Wea. Forecasting,* **2,** 32–49.

——, K. W. Howard, and R. A. Maddox, 1990: Conditions associated with long-lived derechos—an examination of the large-scale environment. Preprints, *16th Conference on Severe Local Storms,* Kananaskis, Amer. Meteor. Soc., 408–412.

Klemp, J. B., and R. B. Wilhelmson, 1978: The simulation of three-dimensional convective storm dynamics. *J. Atmos. Sci.,* **35,** 1070–1096.

Lafore, J., and M. W. Moncrieff, 1989: A numerical investigation of the organization and interaction of the convective and stratiform regions of tropical squall lines. *J. Atmos. Sci.,* **46,** 521–544.

LeMone, M. A., 1983: Momentum transport by a line of cumulonimbus. *J. Atmos. Sci.,* **40,** 1815–1834.

——, G. M. Barnes, and E. J. Zipser, 1984: Momentum flux by lines of cumulonimbus over the tropical oceans. *J. Atmos. Sci.,* **41,** 1914–1932.

Ogura, Y., and M.-T. Liou, 1980: The structure of a midlatitude squall line: A case study. *J. Atmos. Sci.,* **37,** 553–567.

Rotunno, R., J. B. Klemp, and M. L. Weisman, 1988: A theory for strong, long-lived squall lines. *J. Atmos. Sci.,* **45,** 463–485.

Rutledge, S. A., R. A. Houze, M. I. Biggerstaff, and T. Matejka, 1988: The Oklahoma–Kansas mesoscale convective system of 10–11 June 1985: Precipitation structure and single-doppler radar analysis. *Mon. Wea. Rev.,* **116,** 1409–1430.

Smull, B. F., and R. A. Houze, Jr., 1987: Rear inflow in squall lines with trailing stratiform precipitation. *Mon. Wea. Rev.,* **115,** 2869–2889.

Weisman, M. L., 1992: The genesis of severe long-lived bow echoes. *J. Atmos. Sci.,* **49.**

——, J. B. Klemp, and R. Rotunno, 1988: Structure and evolution of numerically simulated squall lines. *J. Atmos. Sci.,* **45,** 1990–2013.

Zhang, D., and J. M. Fritsch, 1988: A numerical investigation of a convectively generated, inertially stable extratropical warm-core mesovortex over land. Part 1: Structure and evolution. *Mon. Wea. Rev.,* **116,** 2660–2687.

Zipser, E. J., 1977: Mesoscale and convective-scale downdrafts as distinct components of squall-line structure. *Mon. Wea. Rev.,* **105,** 1568–1589.